Acta Neuropathologica Communications

RESEARCH

Open Access

Unveiling ribosomal dysfunction and impaired signaling pathways in the cortical region of 5xFAD mice

Kirti Agrawal[1], Blessing C. Egbejiogu[2], Tolulope Adeyelu[3], David Burk[4], Kermit K. Murray[2], Alex Walls[5], Katarina Jones[5], Shawn R. Campagna[5], Joseph Francis[3], Sujoy Ghosh[6], Olalekan M. Ogundele[3] and Manas Ranjan Gartia[1*]

Abstract

Alzheimer's Disease represents the most significant form of neurodegenerative disease worldwide with progressive dementia and synaptic dysfunction. Though the accumulation of β-amyloid and hyperphosphorylated tau protein is the most observed pathological feature of AD, the emergence of ribosomal dysfunction and oxidative stress has recently gained interest. In this study, we conducted a comprehensive multi-omics investigation, which included transcriptomic, proteomic, and lipidomic analyses, on cortical region from 5xFAD mice, a transgenic model of AD. Gene and protein expression analysis demonstrated ribosomal pathways were largely affected in the cortex. Histological and immunohistochemistry imaging showed increased amyloid-β and tau pathology leading to extensive cortical neurodegeneration. RNAseq analysis revealed increased oxidative RNA damage, indicating a potential mechanism of ribosomal stress. Elevated expression of RPL11, RPL6, and other large ribosomal subunit proteins was observed, consistent with impaired protein synthesis. This dysregulation may contribute to neurodegenerative processes in AD. Among the large subunit ribosomal proteins, Rpl29 were downregulated at the gene expression level in AD, although its protein expression revealed a statistically insignificant rise. Comparison between the transcriptome and proteome demonstrated evidence of impaired translation, suggesting failed translational control. Lipidomic analyses revealed alterations in the levels of phospholipids, sphingolipids and lipid mediators in AD that is closely linked to the alterations in the neuroinflammatory pathways at the transcriptomic and proteomics levels. Multi-omics integration demonstrates that ribosomal dysregulation, oxidative stress, and protein homeostasis are affected, leading to neuronal damage in AD. According to this study, ribosomal malfunction plays a significant role in the pathophysiology of AD and serve as a potential target for therapeutic interventions.

*Correspondence:
Manas Ranjan Gartia
mgartia@lsu.edu
[1]Department of Mechanical and Industrial Engineering, Louisiana State University, Baton Rouge, LA 70803, USA
[2]Department of Chemistry, Louisiana State University, Baton Rouge, LA 70803, USA
[3]Department of Comparative Biomedical Sciences, Louisiana State University School of Veterinary Medicine, Baton Rouge, LA 70803, USA
[4]Cell Biology and Bioimaging Core, Pennington Biomedical Research Center, Baton Rouge, LA 70808, USA
[5]Department of Chemistry, University of Tennessee, Knoxville, TN 37996, USA
[6]Bioinformatics and Computational Biology, Pennington Biomedical Research Center, Baton Rouge, LA 70808, USA

Introduction

Alzheimer's disease (AD) is a progressive neurodegenerative disorder affecting the central nervous system, leading to gradual memory loss, reasoning, and language decline [1–4]. The anatomical features of AD include the deposition of β-amyloid plaque in the extracellular region, neurofibrillary tangles composed of hyperphosphorylated tau protein that is located within the intracellular region, neuroinflammation and oxidative stress [5, 6]. In addition to the amyloid cascade hypothesis other molecular pathways such as mitochondrial dysfunction, iron homeostasis disruption, and ribosomal dysfunction has been proposed for AD [7, 8].

Regulation of protein synthesis is essential to cellular function, especially in the brain, where different cell types, such as oligodendrocytes, astrocytes, and microglia, maintain distinct proteomes and need local translation at locations distant from their cell bodies for vital processes like metabolic support, immunological surveillance, and synaptic pruning [9–13]. Translation of information carried by transcripts is performed by ribosomes, comprising 4 ribosomal RNAs and approximately 80 ribosomal proteins (RPs). While transcriptional control in the brain is well understood, the contribution of specific RPs to protein translation and lipid metabolism is unexplored. This could be important in the brain, where precise spatial and temporal control of protein synthesis is essential for maintaining neuronal networks, astrocyte support and microglial response to pathological stimuli.

The ribosomal proteins serve dual functions by enabling protein synthesis while performing essential cellular roles in cell division, apoptosis and DNA damage repair [14, 15]. The malfunction of ribosomes results in protein misfolding and aggregation which are key factors in multiple neurodegenerative diseases that appear during aging including AD [16]. Ribosomes are macromolecular machines that are primarily synthesized within the nucleolus and are essential organelles responsible for protein synthesis [17]. Many studies have also emphasized the importance of ribosomal function in the regulation of neuronal functions [18, 19]. Alterations in the rRNA and tRNA have been found to be related to enhanced oxidative stress and dysfunctional protein homeostasis which worsen the neurodegenerative processes in AD [20, 21]. It has also been shown that oxidative damage of ribosomal proteins is related to the increased RNA oxidation, which in turn exacerbates cellular pathology in the brain of AD patients [22]. However, the method by which dysregulated ribosomes mediate neurodegeneration in AD remains largely understudied [23, 24]. The disruption of degradation processes affects translation dynamics and co-translational processing which results in decreased cellular fitness [23]. Several studies have suggested that the aggregation of nascent proteins and misfolding of co-translated proteins leads to neurodegeneration [25–27]. This pathological process leads to the development of neurological disorders [28–30].

Recently, it was found that, ribosome-related proteins levels of RPL4 and RPS3 expression are reduced in aging tissues [31]. Similar observation of reduced protein synthesis during aging was observed in other studies [32]. However, the opposite is observed in AD, where upregulation of several ribosomal proteins were reported [33]. Abnormal ribosomal protein expression has been demonstrated to occur within both the hippocampal and cortical regions, which suggests that enhanced ribosome function could be associated with AD pathology that are distinct from the typical aging processes [34]. Using multiomics approaches such as transcriptomics, proteomics and lipidomics, we provide a systems-level analysis of the molecular mechanisms that underline AD pathology. We integrate all the omics data to establish a comprehensive picture of the AD pathology, identifying the ribosomal dysfunction as the potential biomarker and the therapeutic target, along with the amyloid β aggregation and tau phosphorylation.

Materials and methods

Animals

The animal studies were in accordance with the Institutional Animal Care and Use Committee (IACUCAM-20-093) at LSU. All relevant ethical guidelines pertaining to animal experimentation and research were followed. 5xFAD mice (Jackson Laboratories, ME, #034840-JAX) were housed in DLAM for 17 months and wildtype C57BL/6 were bred in DLAM, LSU for 6 months. The 5xFAD mice carry five different familial AD mutations (overexpression of mutant human β amyloid (A4) precursor protein 695 (APP) with the Swedish (K670N, M671L), Florida (I716V), and London (V717I)) which cause rapid cognitive decline and severe neuronal damage along with significant β-amyloid accumulation noticeable within several months of development [35–39]. The 5xFAD model shows exceptional value for cortical dysfunction research because the cortical area becomes severely damaged in AD.

Animal brain tissue processing

Mice brains ($n = 10$) were collected from AD ($n = 6$; 5 female and 1 male) and control mice ($n = 4$; all female). Mice undergone deep anesthesia with isoflurane and endured transcardial perfusion with 20 mL of 1xPBS. Brains were extracted on cold surface. Immediately after extraction, the brains were cut into two halves. One half of the brain was fixed using 4% PFA for 3 days followed by storage at 4 °C in a solution containing 30% Sucrose and 4% PFA until further processing. From the other half

of the brain, entire cerebral cortex was isolated and snap frozen at -80°C until further handling.

Cryo-sectioning of cortical regions

The fixed hemispheres brain from the AD ($n = 3$) and control mice ($n = 3$) (all female) were embedded in Tissue-Tek Optimal Cutting Temperature (OCT) solution (Sakura). Sectioning of the tissue were performed using a Leica cryostat. Tissue sections measuring 10 µm and 50 µm in thickness were collected in 96-well plates and stored in 1xPBS and 0.01%Sodium Azide at 4 °C until further processing.

Hematoxylin and Eosin (H&E) staining

Glass slides (Corning) were used to mount 10 µm brain slices embedded in OCT. For histological staining, tissue sections (5xFAD ($n = 3$) and C57BL/6 ($n = 3$); all female mice) were stained with hematoxylin and eosin (H&E) dyes. The staining procedure was performed with Surgipath Sub-X mounting medium on a Leica ST5020/CV5030 autostainer (Leica Biosystems) and Eosin Phloxine 515, SelecTech Hematoxylin 560 were used for staining, along with bluing and define solutions from Leica Biosystems. A NanoZoomer® Slide Scanner System was used to image stained slides. NDP.view was the program used to gather images. And the software is called NDP.view2. ImageJ was used for quantification and GraphPad Prism software for data plotting.

Immunohistochemistry imaging

Immunohistochemical staining was performed to demonstrate the presence and distribution of β-amyloid and tau proteins in tissue sections (5xFAD ($n = 3$) and C57BL/6 ($n = 3$); all female mice). The tissue Sect. (50 µm) were then washed twice in PBSTx-100 for 10 min each time. After the washes, the sections were then blocked with 250 µL of 5% serum in PBSTx-100 for 1 h at room temperature (RT). After that, the sections were placed in wells containing 200 µL of 5% serum with the Alexa Fluor® 488 Anti-β Amyloid 1–42 antibody [Abcam, Cat # mOC64] and Alexa Fluor® 488 Anti-Tau antibody [Abcam, Cat # EP2456Y] and were incubated overnight at 4 °C with gentle shaking at 35 rpm. The following day, the sections were washed twice in PBSTx-100 for 10 min each time. A secondary antibody (1:2000) was diluted in 200 µL of fresh serum and added to the sections, which were then left to incubate for 1 h at RT. The stained tissue slices were mounted on the slides using mounting media with DAPI. Imaging was performed using ZEISS Axioscan 7 microscope images were processed using Zeiss Zen Blue Lite software. ImageJ was used for quantification and GraphPad Prism software for data analysis.

Bulk RNA-sequencing (RNAseq)

The total RNA was extracted from flash frozen cortical tissue of 5xFAD ($n = 3$) and C57BL/6 ($n = 3$) female mice using TRIzol reagent (Invitrogen, USA) and the Qiagen RNeasy Mini Kit (Qiagen, Cat # 217004) for better RNA yield and purity. 1 mL of TRIzol reagent was added to about 50 mg of cortical tissue and then all the samples were thoroughly lysed using a mechanical tissue homogenizer. The homogenized samples were then placed in a centrifuge at 15,000 g for 15 min at 4 °C and the supernatant which contains the RNA was then collected. To begin the phase separation process, the samples were placed at room temperature for 5 min and then chloroform (140 µL) was added to the samples. The tubes were then vigorously shaken for 15 s and then briefly incubated and then centrifuged at 12,000 g for 15 min at 4 °C. When the centrifugation was done, the aqueous phase which contains the RNA was then collected to avoid contamination with the interphase and organic layer. An equal volume of 100% ethanol was added to the lysate and the mixture was transferred to a RNeasy Mini Column (Qiagen). The RNA was then bound to the column and washed with the buffers provided in the Qiagen kit as recommended by the manufacturer. The elution of the purified RNA was done using 30 µL of RNase free water to give high purity total RNA that can be used for subsequent bulk RNA sequencing. Nanodrop Spectrophotometer ND-1000 UV/vis was used to determine the concentration and purity of the RNA and extracted high quality RNA were then shipped to Novogene (https://www.novogene.com/us-en/) for Bulk RNA sequencing on the Illumina platform [40]. cDNA library construction was performed with 1 µg of RNA using NEBNext Ultra 2 RNA Library Prep Kit for Illumina (cat NEB #E7775, New England Biolabs, Ipswich, MA, USA) according to the manufacturer's protocol. The mRNA were enriched using oligo (DT) beads and followed by two rounds of purification and fragmented randomly by adding fragmentation buffer. The first strand of cDNA was synthesized using the random hexamers primer. Next, dNTPs, RNase H, DNA polymerase 1, and a custom second strand synthesis buffer (Illumina) were added to produce the second strand (ds-cDNA). Subsequently, terminal repair, poly-adenylation, and sequencing adaptor ligation were performed, followed by size selection and PCR enrichment. This resulted in 250–350 bp insert libraries, which were quantified using a Qubit 2.0 fluorometer (Thermo Fisher Scientific, Walkham, MA, USA) and quantitative PCR. An Agilent 2100 Bioanalyzer (Agilent Technologies, Santa Clara, CA, USA) was used to determine size distribution. Sequencing was performed on an Illumina NovaSeq 6000 Platform (Illumina, San Diego, CA, USA) using a paired-end 150 run (2 × 150 bases) Q30 ≥ 80% at

20 M raw reads/sample. Alignment was performed using hisat2, v2.1.

Proteomics

Tissue microsampling was performed using an infrared (IR) laser ablation (Figure S1) (5xFAD (n = 3) and C57BL/6 (n = 3); all female mice) and capture system that has been described previously [41]. The system comprises an OPO laser (Opolette 2940, OPOTEK, Carlsbad, CA, USA), focusing optics, attenuation, and sample collection system. The OPO was operated at 2940 nm wavelength, 20 Hz repetition rate, and was focused to a spot size of 50 µm for tissue ablation in transmission geometry. The tissue section was translated horizontally at 600 µm/s in a serpentine pattern with a 30 µm line spacing, corresponding to 1.5 shots per spot. Areas of 1 mm^2 cortex were ablated from 5xFAD mice (n = 3) and healthy C57BL/6 mice (n = 3) brain samples and captured. Ablated tissue was collected in 0.2 µL dimethyl sulfoxide (DMSO; Mallinckrodt) on a PTFE printed glass microscope slide (Electron Microscopy Sciences, Hatfield, PA, USA). The capture slide was placed at ca. 1 mm below the tissue and translated using a three-dimensional micrometer-driven stage (Model-423, Newport, Irvine, CA, USA). After ablation, the capture slide was stored at − 20 °C prior to protein digestion.

Protein digestion on the capture slide followed a previously reported method [42]. Initially, the slides were brought to room temperature, and 500 nL of a solution consisting of 10 mM DL-dithiothreitol (DTT; Sigma-Aldrich) and 0.2% n-dodecyl-β-d-maltoside (DDM; Sigma-Aldrich) in 100 mM ABC buffer was introduced into each microwell. Subsequently, the slide was placed in a small aluminum box (12 × 9 × 3 cm) with a layer of water at the bottom to maintain humidity and incubated for 1 h at 90 °C in a gravity convection oven (Cat # 89511-404, VWR) to reduce disulfide bonds. The slide was vacuum-dried, and a solution containing 30 mM iodoacetamide (IAA; Sigma-Aldrich) in 100 mM ABC buffer was added to each microwell. To achieve protein alkylation, a plain microscope slide with a 1 mm spacer was placed over the samples in a Petri dish (10 cm diameter and 1.5 cm depth) with a water layer at the bottom to maintain humidity, and the slide was incubated in darkness at approximately 25 °C for 30 min. Protein digestion was achieved by adding 500 nL of 2.5 ng trypsin/Lys-C mix (Promega, Madison, WI) in 100 mM ABC to each microwell, replacing the cover, and incubating in the Petri dish overnight at 37 °C in a gravity convection incubator (Cat # 89511-420, VWR). Finally, 500 nL of 2% formic acid was added to each microwell to quench the digestion, and the capture slide was vacuum-dried and stored at − 20 °C until mass spectrometry analysis.

Before LC-MS/MS analysis, the PTFE slides were equilibrated to room temperature, and the dried protein digest was rehydrated with 3.5 µL of 0.1% formic acid, then transferred to a 0.2 ml microcentrifuge tube. The microwells on the capture slide were rinsed with an additional 3.5 µL of 0.1% formic acid, resulting in a total volume of 7 µL. This peptide solution underwent centrifugation at 10,000 g for 10 min, and 5 µL of the supernatant, avoiding tissue debris, was pipetted into a 250 µL polypropylene microvial (Cat # 66021-194, VWR). The chromatographic mobile phase consisted of 0.1% aqueous formic acid (Solvent A) and 0.1% formic acid in ACN (Solvent B). The sample was loaded onto an Acclaim PepMap 100 C18 trap cartridge (0.3 × 5 mm, 5 µm particle size, 100 Å pore size) at a flow rate of 10 µL/min for 10 min using 5% Solvent B. Separation occurred on an Acclaim PepMap 100 C18 nanoLC column (75 µm × 15 mm, 3 µm particle size, 100 Å pore size) with a linear gradient from 5% to 45% Solvent B over 60 min at a flow rate of 300 nL/min.

LC-MS/MS was carried out using an Ultimate 3000 RSLC liquid chromatography system coupled to an Orbitrap Q-Exactive mass spectrometer (Thermo Fisher Scientific, Waltham, MA). The mass spectrometer operated in data-dependent acquisition mode, encompassing a full MS scan range of 300–1800 m/z, a resolution of 70,000, an automatic gain control AGC target of 1×10^6, and a maximum injection time of 30 ms. After each MS1 scan, the 10 most abundant precursor ions with charges between + 2 and + 7 and intensity exceeding 1×10^4 were selected with a m/z window of 2, a 5×10^4 AGC target, 50 ms maximum injection time, 60 s dynamic exclusion, and subjected to fragmentation via high energy collision at 30% normalized collision energy. MS/MS spectra were captured at a resolution of 17,500.

Identification and quantification of protein levels was performed via the Proteome Discoverer (ver. 2.4, Thermo Fisher Scientific, Waltham, MA), employing both Sequest HT and Mascot (Matrix Science, London, UK) search engines. The search was performed against the UniprotKB database (Release 2020_06) with taxonomy restricted to Rattus norvegicus. Methionine oxidation (dynamic) and cysteine carbamidomethylation (static) were selected as peptide modifications, while dynamic protein modifications included N-termini acetylation, methionine loss, contemporary acetylation, and methionine loss. The endopeptidase trypsin Lys-C was chosen with a maximum of 2 missed cleavages. Spectrum selection employed a 1.5 signal-to-noise threshold, and mass tolerances were set at 10 ppm for precursors and 0.2 Da for fragments. The minimum peptide length was six amino acids. Peptide spectrum match validation employed Percolator software with a target false discovery rate (FDR) of 0.01 (strict) and 0.05 (relaxed). A

consensus workflow was subsequently utilized to further process the result files, yielding protein identification and quantification. Proteins were considered identified if they had at least two matching peptides, including one unique peptide, with a minimum FDR of 0.05.

Lipidomics

UHPLC-HRMS methods: Global lipidome profiling was performed using an established HILIC method [43]. The 5xFAD (n = 6; 5 female and 1 male) and control (n = 4; all female) samples were stored at 4 °C prior to analysis. A Thermo Fisher Scientific, Waltham, MA -Vanquish ultra-high performance liquid chromatography system (UHPLC, Waltham, MA) was used to inject 5 µL of sample onto an Acuity UPLC BEH HILIC column (1.7 µM, 2.1 mM X 100 mM; Waters). Mobile phase A consisted of acetonitrile/water (50:50, v: v) while mobile phase B consisted of acetonitrile/water (95:5), each with 10 mM ammonium acetate and adjusted to pH 8. The gradient was linear from 100% to 80% A in 10 min at flow rate of 500 µL/min and column temperature of 30 °C The gradient used was as follows: t = 0 min: 100% solvent B flow rate of 0.50 mL/min, t = 10 min: 80% solvent B flow rate 0.5 mL/min, t = 10.0 min: 100% solvent B flow rate 0.5 mL/min, t = 11 min: 100% solvent B flow rate 0.5 mL/min until equilibration at 11 min. Eluent was introduced to the mass spectrometer via heated electrospray ionization (HESI) source, with the following parameters: sheath gas 50 (arbitrary units), aux gas 10 (arbitrary units), sweep gas 0 (arbitrary units), spray voltage 3.5 kV (positive), 2.5 kV (negative), ion transfer tube temperature 325 °C . Mass analysis was performed using an Orbitrap Exploris 120 (Thermo Scientific, Waltham, MA) mass spectrometer. Each sample was analyzed in both positive and negative polarity modes utilizing the same chromatographic method. Ions of PC species were detected in positive mode with PG and PE detected in negative mode. Masses were detected in full scan mode within a scan range of 100–1,000 m/z, operated at a resolution of 120,000, with an automatic gain control target of (AGC) of 3×10^6 ions, and a maximum injection time of 100 ms. Full scan data was complemented with data dependent acquisition (DDA) at a resolution of 35,000 utilizing 35 eV collisional energy. The mass spectrometer was calibrated every 24 h. Based on an internal standard, the retention time for each GP class is as follows: PA 5.94 min, PC, 5.16 min, PE 4.17 min, PG 1.76 min, PI 3.67 min, PS 5.8 min.

Identification and quantification of glycerophospholipids (GP) and free fatty acids (FA) were identified using a custom library 1700 GP structures, retention time matches deuterated internal standards (+/- 0.5 min), and mass accuracies (+/- 5 ppm) of the expected m/z values using an Orbitrap Exploris 120. The deuterated internal GP standard included 15:0–18:1(d7) PC160, 15:0–18:1(d7), 15:018:1(d7)PS5, 15:0–18:1(d7) PG30, 15:0–18:1 (d7) PI10, 15:0–18:1 (d7) PA7, 18:1 (d7) LPC25, 18:1 (d7) LPE5, 18:1 (d7) Chol Ester350, 18:1 (d7) MG2, 15:0–18:1 (d7) DG10, 15:0–18:1 (d7)-15:0 TG55, 18:1(d9) SM30, and cholesterol (d7) 100. Glycerophospholipids predominately ionized as [M-H]- in negative mode and [M] + in positive mode for phosphatidylcholine (PC) using heated electrospray ionization for a hydrophilic interaction liquid chromatography (HILIC) method. RAW data acquired from XCalibur (version 4.2 SP1, Thermo Fisher Scientific) were converted to a .mzML format using MS convert (ProteoWizard). El MAVEN analysis package (V0.12.0) was used to manually integrate exact masses and ion intensities of predicted GP species with an error < 5 ppm [44–46] The integrated intensities were normalized to a known concentration of the deuterated internal standard that allowed for the average peak area, standard deviation, and individual concentration of GP to be calculated. GP abundances were calculated by summation of the relative concentrations by comparison to the Avanti deuterated internal standard. Heatmaps were developed in RStudio (V2024.12.1) that summed GP species and calculated the ratio of normalized, $\log_2$ transformed intensities of experimental group over the control group. A paired student's t-test was utilized to determine significance can calculate p-values. Abundance data represent the averages of three biological replicates. The EICs and mass spectra were plotted using XCalibur software version 4.2 SP1 (Thermo Fisher Scientific, Waltham, MA).

Bioinformatics analysis

The transcriptomics, proteomics and metabolomics data were subjected to individual bioinformatics data analysis pipelines as described below. For the transcriptomics data, the FASTQ formatted RNA sequencing files were decompressed and sequencing reads were quality-checked via the RseQC (version 5.0.3) [47], adapter trimmed using Cutadapt [48], mapped to the mouse reference genome (GRCm39) via STAR (version 2.7.11b) [49], and converted to raw counts with featurecounts from the RSubreads (version 2.20.0) [50]. After removal of low expressing genes, 15,500 genes were retained (from an original 47626 genes). Raw counts were normalized via the TMM-normalization method in the edgeR package (v. 3.38.4) [51], with normalization values ranging between 0.91 and 1.06. Principal component analysis was conducted using princomp function in R for outlier detection (none detected). Differential gene expression analysis was performed via the limma package using the trend function (version 3.56.1) [52], and genes with an adjusted P value (FDR) ≤ 0.05 were considered as differentially expressed (DEG), unless otherwise indicated. Gene-set enrichment analysis was performed via the Fast

Gene Set Enrichment Analysis (fGSEA) (v. 1.30.0) package [53], based on gene set permutations on a pre-ranked gene list to identify enrichment of pathways present in the Kyoto Encyclopedia of Genes and Genomes database (KEGG), available from the Molecular Signature Database (MSigDB) [54] repository. Pathways with adjusted P values ≤ 0.05 were considered to be significantly regulated. The direction of pathway regulation was determined by the sign of its normalized enrichment score statistic (NES) derived from fGSEA with a positive NES indicating pathway upregulation with respect to the comparator group.

The proteomics data consisted of 884 proteins with full expression results, and after removal of low-expressed proteins, 828 proteins were retained for further analysis. Protein levels were normalized to total input proteins. Principal components analysis identified no outlier samples. Differential expression analysis was performed via limma. Due to the reduced coverage of the proteome by the lower number of proteins (compared to the transcriptome), a pathway overrepresentation analysis of KEGG pathways was conducted via Enrichr [53] instead of fGSEA [55]. Pathways with an overrepresentation FDR ≤ 0.05 were considered to be significantly regulated.

The lipidomics (phospholipids plus lipid mediators) dataset was normalized against internal standards for all lipids except lipid mediators. Further analysis of lipidomics data was conducted through the web-version of Metaboanalyst 6.0 (https://www.metaboanalyst.ca/MetaboAnalyst/) [56] via the one-factor statistical analysis option. To ensure proper normalization, the metabolite expression data was further log10 transformed and median normalized for all lipids excepting lipid mediators (lipid mediators were found to be sufficiently normalized after log10 transformation alone). Principal components analysis was performed separately on lipids and lipid mediators and no outlier samples were detected. Both univariate (t-test and Wilcoxon test) and multivariate (partial least squares discriminant analysis or PLSDA) were conducted to identify individual metabolites or groups of metabolites that contributed to a differentiation between control and 5xFAD samples. For PLSDA analysis, a variable importance plot (VIP) was further constructed to identify top metabolites (variables) contributing to discrimination between the groups.

Results

Histopathological and morphological analysis of cortical regions

The experimental workflow presented in Fig. 1a showed the research design for analyzing cortical areas of AD and control mice. The H&E evaluation (Fig. 1b) revealed considerable neuronal cell loss in the cortical areas of 5xFAD mice as compared to the healthy controls. In the healthy controls, neurons had intact architecture and were easily distinguishable while 5xFAD mice had disrupted cortical architecture along with the β-amyloid plaques and tau tangles (Fig. 1b). Image analysis showed that the cortical region significantly reduced ($p = 0.0154$) in the AD brain (Fig. 1c).

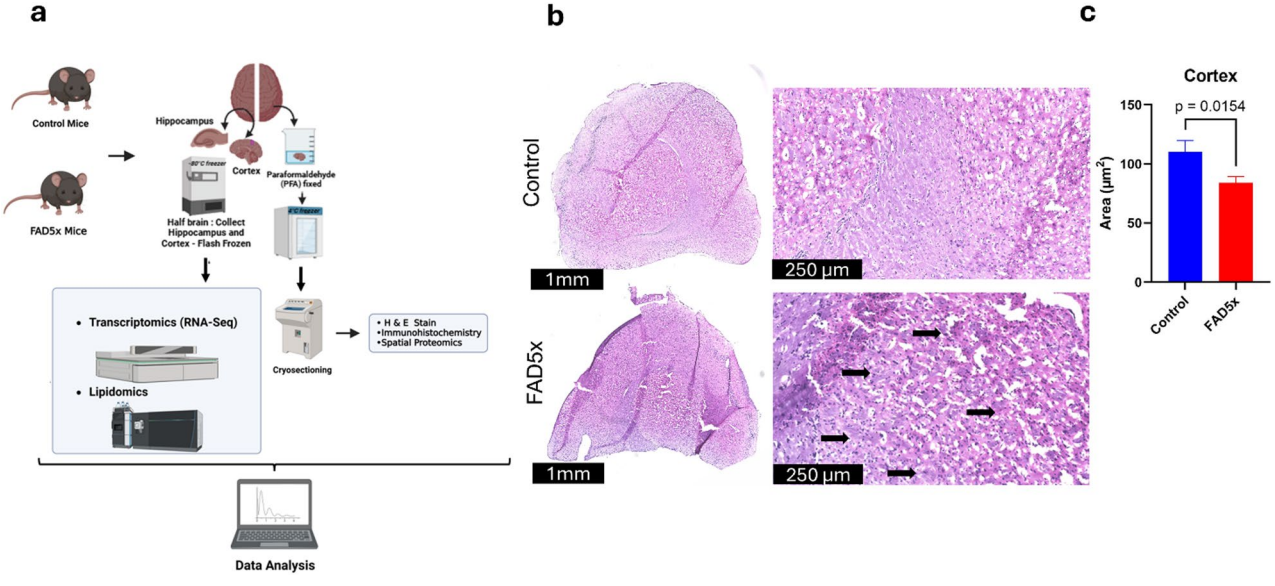

Fig. 1 (a) Schematic (created with http://www.biorender.com/) of the experimental workflow. (b) Comparative histological and morphological assessment of the cortical region in Control and AD mice. The black arrow shows β-amyloid plaques in the cortical region of 5xFAD mice. (c) Quantitative analysis of the area of the cortical region for control and 5xFAD brain

Immunohistochemical (IHC) detection of β-amyloid and Tau proteins

The immunohistochemical imaging of cortical regions of AD and control mice demonstrates the increased deposition of β-amyloid (Fig. 2a) and tau (Fig. 2b) proteins, in AD as compared to the control mice. The quantitative fluorescence intensity analysis (Fig. 2c and d) showed significant intensity and % coverage of both the proteins (β-amyloid and tau) in the AD group as compared to the control group.

Transcriptomic and proteomic profiling

To access the differences in the transcriptomic and protein expression of AD mice, bulk RNA sequencing and proteomics analysis were performed on the 5xFAD and the control samples. For the proteomics analysis selected brain region(cortex) were laser ablated from the entire brain tissue. Data was subjected to analysis of DEGs and DEPs at FDR ≤ 0.05. Volcano plots identified genes and proteins that were significantly up-regulated and down-regulated in AD (Fig. 3a and b). Boxplots were constructed for top 10 most differentially expressed genes (Figure S2c) and proteins (Figure S6a) (FDR ≤ 0.05). The hierarchically clustered heat maps (Fig. 3c & 3d) display the sample-level expression of the top 50 DEGs and DEPs (selected based on FDRs), respectively. The bar graph (Fig. 3e) shows the differentially expressed genes and proteins for the transcriptomic and proteomic datasets. The transcriptomic data had 691 up-regulated and 600 down-regulated genes while the proteomic data had 152 up-regulated and 110 down-regulated proteins (both at FDR ≤ 0.05). The differences in the number of

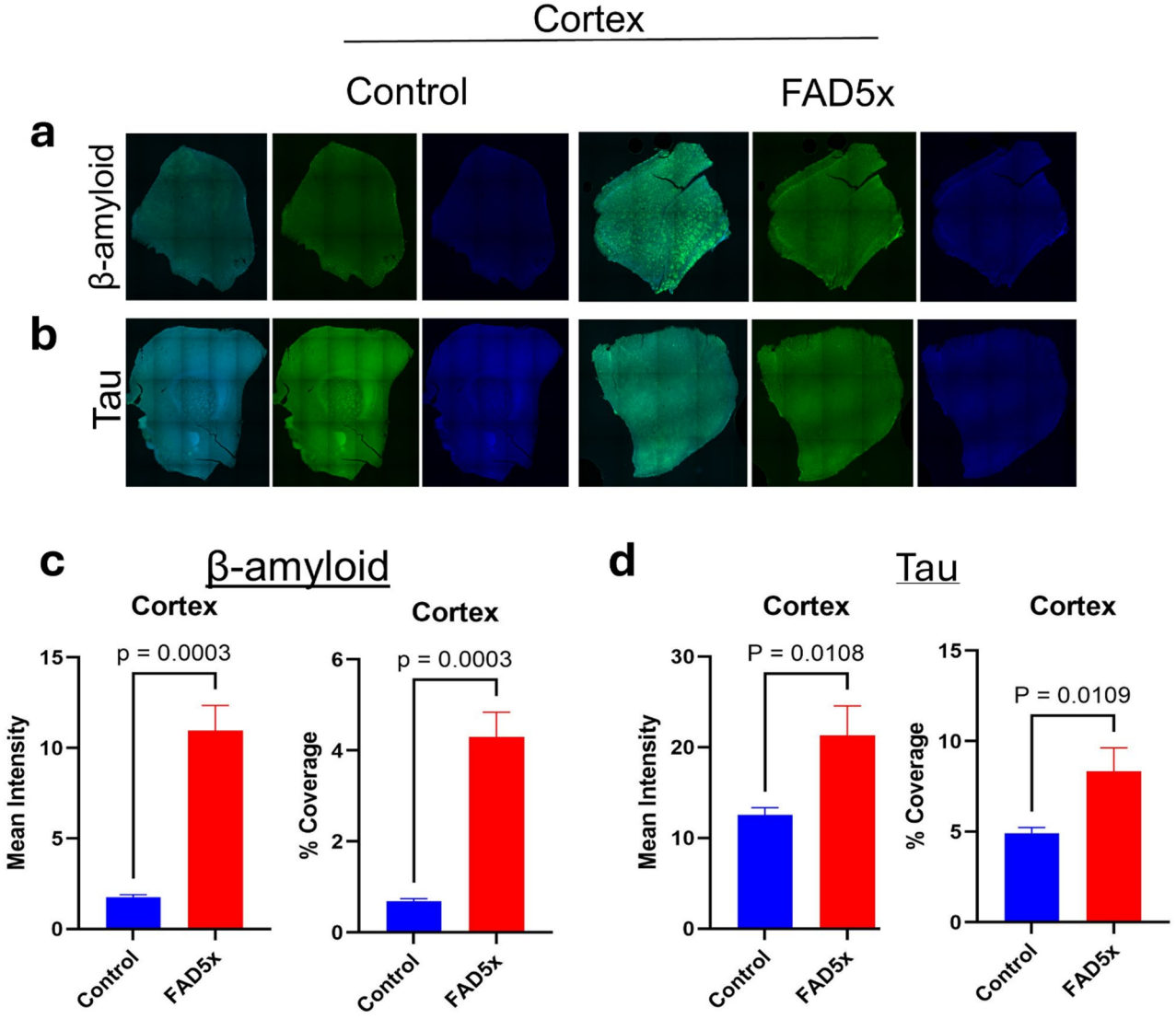

Fig. 2 Comparison of the fluorescence image of the cortex region of the brain for control and 5xFAD mice, illustrating the distribution of **a**β amyloid and **b** tau proteins, respectively. Mean intensity and coverage % of **c** amyloid-β, and **d** Tau protein in the cortex region

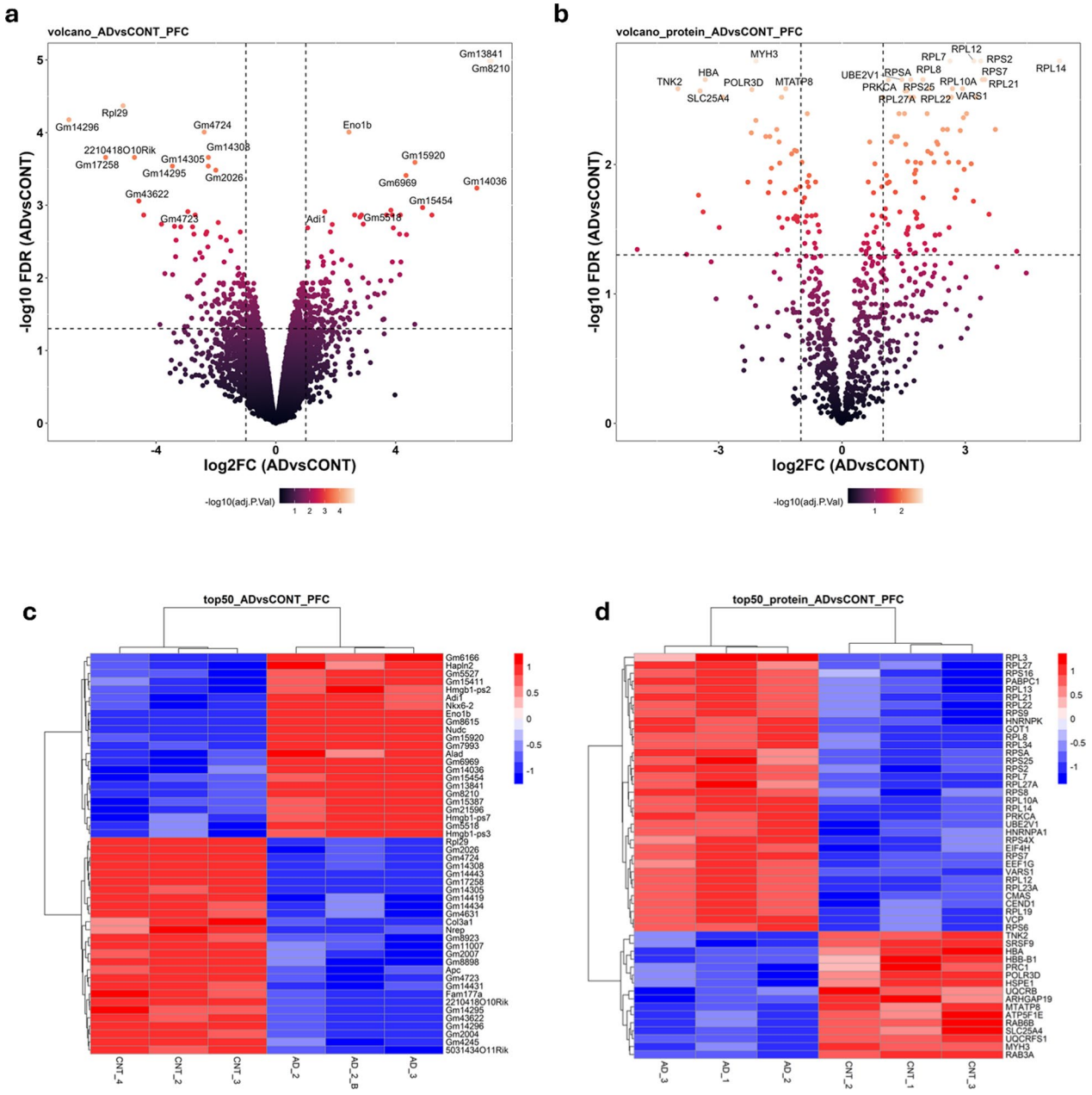

Fig. 3 Volcano plot showing the upregulated and downregulated genes in the cortex at the **a** transcriptomic and **b** proteomic level, respectively. Heatmap showing the top 50 **c** differentially expressed genes (DEGs) and **d** differentially expressed proteins (DEPs, (based on FDR) in the cortex region. Red shows upregulation whereas blue shows downregulation. For each gene/protein, expression levels are row-normalized and expressed via a color scale ranging from blue (lower expression) to red (higher expression). **e** Summary of total number of genes and proteins significantly upregulated and downregulated (FDR ≤ 0.05) in the cortex of AD and control. **f** Venn diagram illustrating the overlapped DEGs and DEPs in the cortical region of the brain (FDR ≤ 0.05). **g** Heatmap of sample-level expression profiles for the common list of significantly differentially expressed (FDR ≤ 0.05) genes and proteins in AD and control samples. All expression levels are row-normalized and expressed in a color scale from blue (lower expression) to red (higher expression). The first six columns of the heatmap refer to protein expression whereas the last six columns represent gene expression data

differentially expressed genes and proteins is primarily a reflection of the much bigger pool of gene candidates considered for differential analysis (15,500) compared to proteins (828). A comparison of the significantly differentially expressed (FDR ≤ 0.05) genes and proteins (Fig. 3e)), identified an overlapping set of 25 common DEGs and DEPs, including several proteins associated with the large (60 S) and small (40 S) subunits of the eukaryotic ribosome (RPL14, RPL8, RPL21, RPL34, RPL3, RPL27A, RPL19, RPL13, RPL23A, RPL4, RPL11, RPL13A, RPS25, RPS8, RPS11, RPS3 and RPS23, RPS10, RPS18, RPS6) as well as other proteins (EEF1G, SOD1, ATP6V1G1,

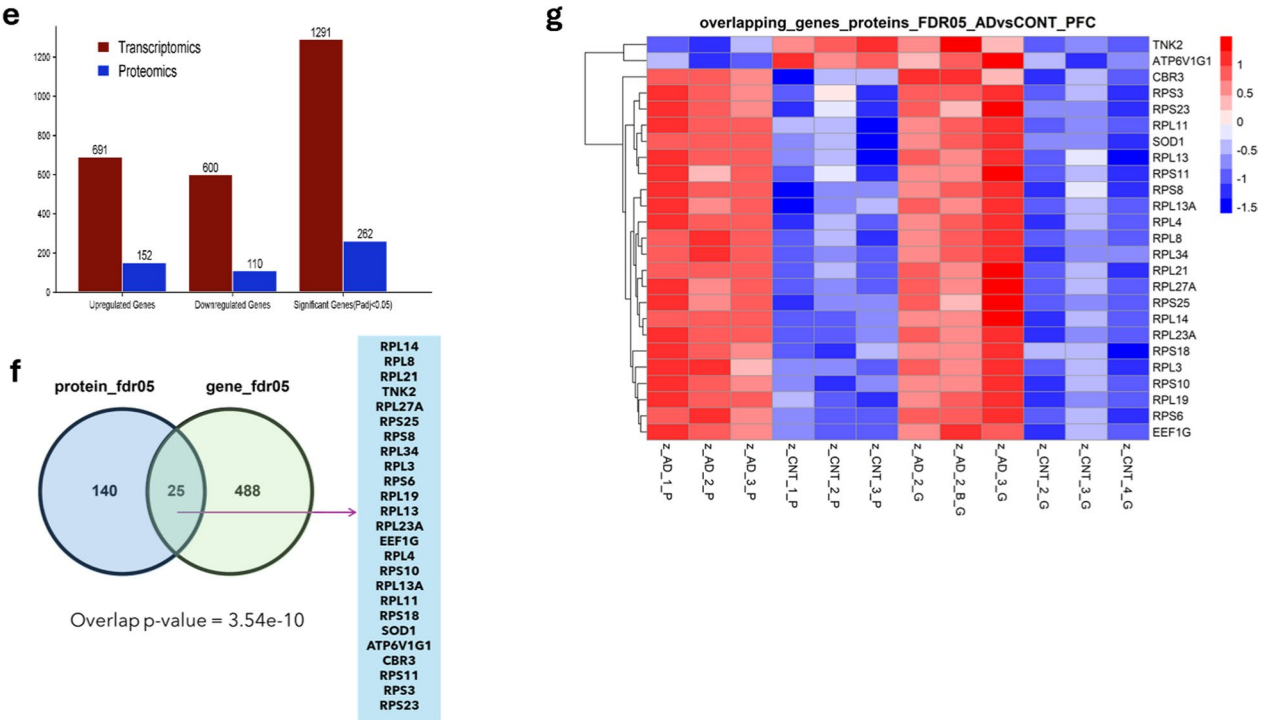

Fig. 3 (continued)

CBR3, and TNK2). The heatmap (Fig. 3g) shows the sample-level expression of these common genes and proteins and displays wide concordance in their levels of expression between the AD and control groups with the exception of TNK2 and ATP6V1G1. These two genes were upregulated in AD compared to controls, but their corresponding protein expression was downregulated in AD samples.

Ribosomal pathway dysregulation

The analysis of the RNA seq data reveals a significant dysregulation of the ribosomal pathway and other important biological processes. Principal Components Analysis (PCA) (Figure S2a) was performed on normalized transcriptomic data after removal of low expressing genes. Samples were color-coded by group (AD, CNT). Clear separation between groups was observed, first 2 principal components explain ~ 62% variation in gene expression.

Nominal p-values obtained from differential gene expression analysis via limma (Figure S2b). Histogram shows the gene counts at each *p*-value bin. Total of 20 bins, with each bin representing a p-value change of 0.05 and first bin (0-0.05) represents genes with strongest evidence for differential expression between AD and Control. Boxplots (Fig. 4a) show that several ribosomal protein genes (Rpl family) are consistently upregulated in the AD group as compared to controls, which suggests that there is an increase in ribosomal activity or biogenesis. The only exception was Rpl29 which was significantly downregulated in the AD samples (although protein levels of RPL29 were not significantly different between AD and controls). While the important of this selective transcriptomic difference in regulation is currently unclear, it may point to an attempt at selective ribosome remodeling via transcriptional regulation leading to ribosome assembly with different RPL compositions in AD and control samples [57]. Pathway enrichment analysis conducted via FGSEA on KEGG pathway database (Figure S3a), wiki pathway database (Figure S3b), and hallmark pathway database (Figure S3c) for AD vs. Control (FDR ≤ 0.05).

The GSEA enrichment plot for the Ribosomal pathway from the KEGG database (Fig. 4b) also supports this finding with a highly significant enrichment score (NES = 2.62, $p = 0$) and a clear bias towards the upregulation of ribosomal genes in the AD group. Figure 4c shows the full list of KEGG pathways that were significantly enriched (up- or down-regulated) in the AD compared to control samples, with the Axon Guidance, Oxidative phosphorylation and Ribosomal pathway showing the highest level of statistical significance among the AD-upregulated pathways. Other affected pathways include biological processes related to antigen processing, lysosomes, and inflammatory signaling, suggestive of effects on protein synthesis, immune response, and cellular signaling.

To analyze the translation of these transcriptome, we performed unbiased proteomic analysis of the cortex region in the AD and control samples. The proteomic

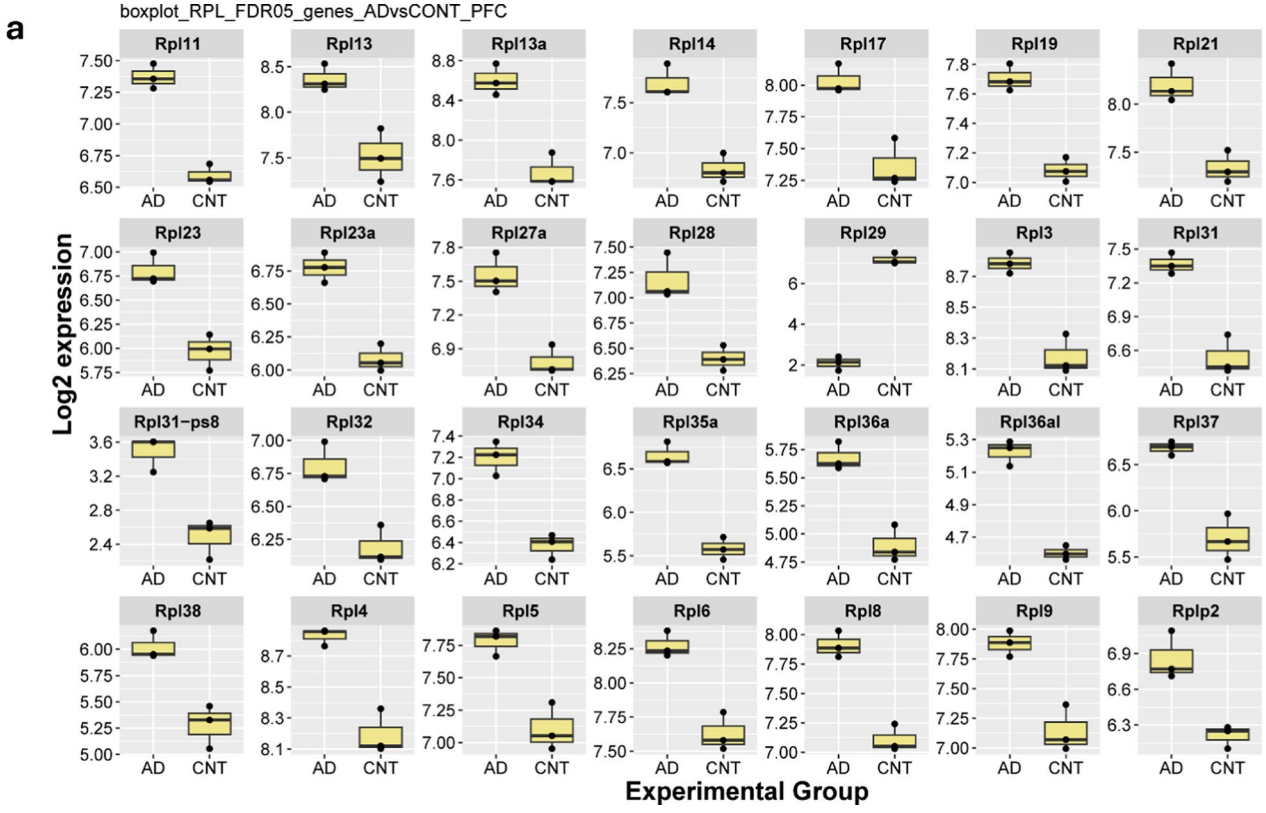

Fig. 4 **a** Boxplots depicting the distribution of expression for different ribosomal protein L isoform coding genes (RPLs) with FDR ≤ 0.05 in AD and control samples. **b** fGSEA derived enrichment plots for the KEGG- Axon Guidance, Oxidative phosphorylation and Ribosome pathway. The normalized enrichment score (NES) and nominal enrichment p-value are shown in the plot inset. **c** Pathway enrichment using KEGG showing pathways that are significantly regulated between AD and control samples (FDR ≤ 0.05). The length of the bars indicated the magnitude of pathway enrichment whereas the color of the bar is proportional to the evidence for statistically significant difference (darker shade indicating greater statistical significance); **d** GO enrichment analysis of significant (Padj ≤ 0.05) DEGs; **e** Network visualization showing the relationship between the differentially expressed genes and their associated pathways using SRplot

analysis showed increase expression of all RPL proteins in AD except for RPL29 (Figure S6) significantly. Gene Ontology pathway enrichment analysis [58] identified the major biological processes, molecular functions, and the cellular component pathways for DEGs (Fig. 4d) in the RNA seq data, along with the KEGG pathway enrichment plot (Figure S4a, S4b, S4c). The network visualizations depicted GO term relationships with their associated genes through node size indicating linked gene numbers and edge color representing functional categories (Fig. 4e).

The proteomic analysis showed that all RPL proteins demonstrated increased expression in AD group. Principal Components Analysis (PCA) (Figure S5a) was performed on normalized transcriptomic data after removal of low expressing genes. Samples were color-coded by group (AD, CNT). Clear separation between groups was observed, first 2 principal components explain ~ 64% variation in gene expression. Nominal p-values obtained from differential gene expression analysis via limma (Figure S5b). Histogram shows the gene counts at each *p*-value bin. Total of 20 bins, with each bin representing a p-value change of 0.05 and first bin (0 - 0.05) represents genes with strongest evidence for differential expression between AD and Control.

The analysis revealed that RPL11, RPL15, RPL24 and RPL8 showed significant overexpression in AD samples (FDR ≤ 0.05) as shown in Fig. 5(a). The ribosome pathway together with cysteine and methionine metabolism and protein processing in endoplasmic reticulum pathways showed significant overrepresentation among differentially expressed proteins in AD (Fig. 5b). The KEGG pathway analysis (Fig. 5c) showed substantial changes in oxidative phosphorylation neurodegeneration pathways, which include Alzheimer's disease, synaptic pathways, and calcium signaling (Figure S7). The results show that RPL isoform dysregulation in AD could lead to extensive changes in metabolic and stress response and translational pathways which demonstrates the essential role of ribosome-associated functions in AD molecular pathogenesis. Gene Ontology pathway enrichment analysis [58] identified the major biological processes, molecular

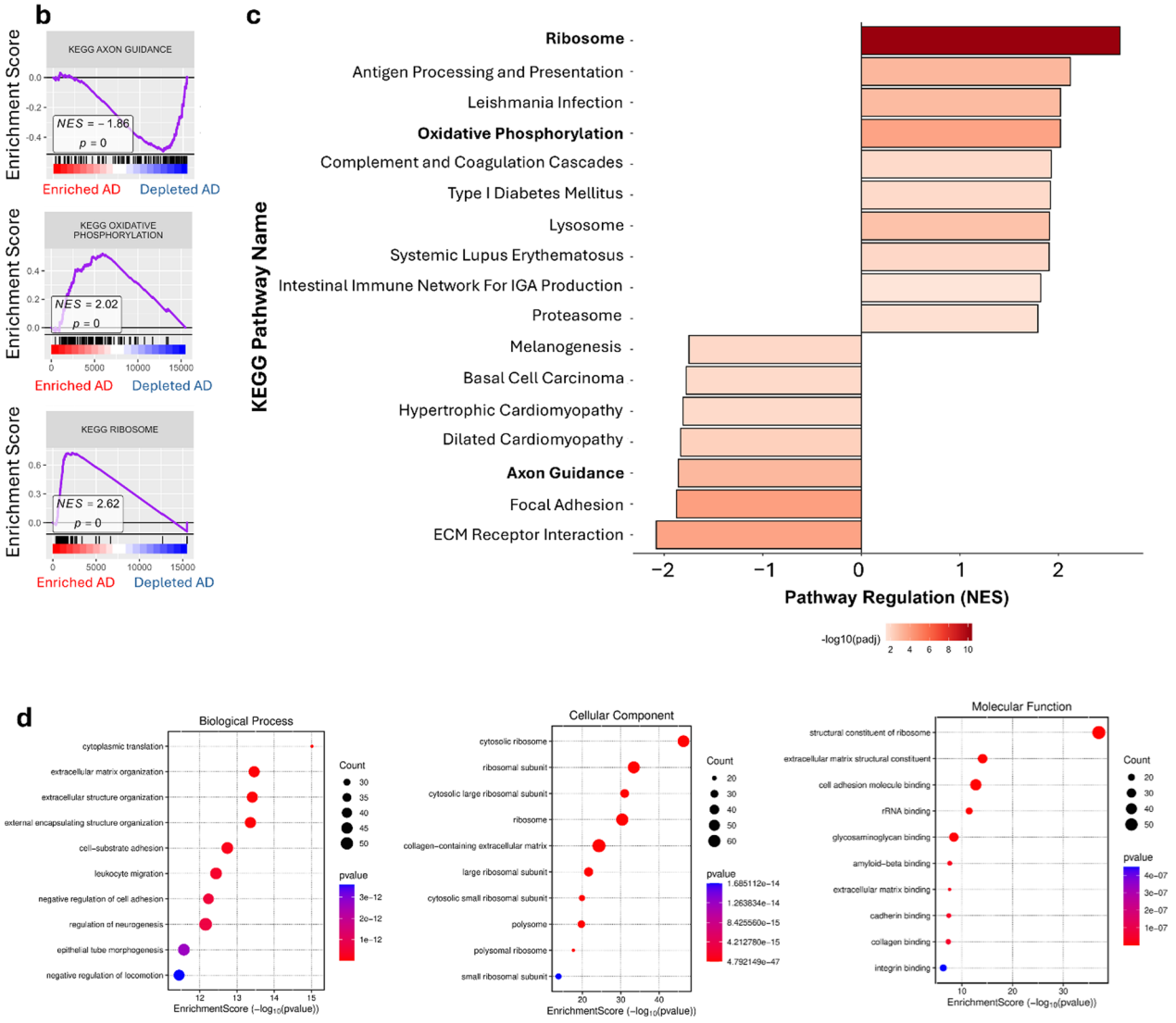

Fig. 4 (continued)

functions (Fig. 5d), and the cellular component pathways (Fig. 5e), considering all the DEPs and considering only the upregulated (Figure S7) proteins in the proteomics data.

The evaluation of AD transcriptomic and proteomic changes requires pathway enrichment analysis of both datasets followed by result integration (Fig. 6). The Venn diagrams show the overlapping and separate pathways that exist between upregulated and downregulated genes and proteins in the AD and control samples. The upregulated pathways that appear in both datasets include ribosome and mRNA processing (WP310) and cytoplasmic ribosomal proteins (WP163) and adipogenesis and Myc targets V1 and coronavirus disease. The analysis revealed 4 pathways that appeared only in the transcriptome data and 15 pathways that appeared only in the proteome data. The Ras signaling pathway and calcium signaling pathway showed consistent downregulation in both transcriptomic and proteomic data, but 9 pathways appeared only in the transcriptome and 7 pathways appeared only in the proteome. The results show that ribosome activity and mRNA processing show uniform elevation but neuronal signaling pathways demonstrate consistent deterioration between the two molecular layers.

The combination of transcriptomic and proteomic data revealed matching pathway patterns between essential disease-related modules (Fig. 6a and 6h). The mitochondrial dysfunction pathway (Fig. 6a and 6e) contained 48 genes (Figure S8a & S8b) which shared 7 common elements between datasets including altered protein levels of NDUFA6/4/2, CHCHD3, CYB5B and DNM1 as compared to gene data set. The protein-level impairment of oxidative phosphorylation received partial transcriptional compensation according to these results. The

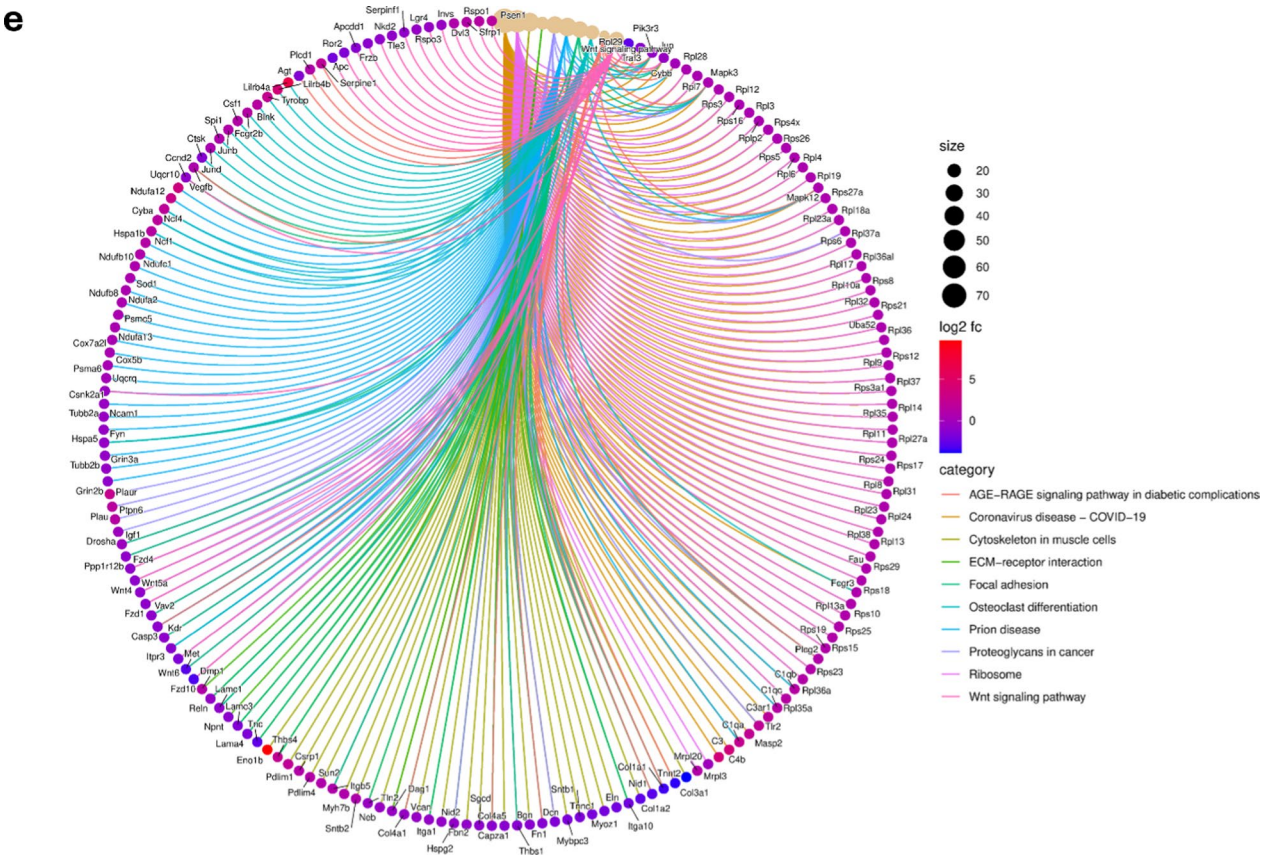

Fig. 4 (continued)

synaptic dysfunction pathway (Fig. 6b and 6f) contained 40 genes (Figure S9a & S9b) which shared 15 common elements that showed decreased protein levels of SYNGAP1, GRIN1, STX1A/2, CAMK2A, MAPT SYNPO and PCP4 despite minimal RNA changes. The protein levels of synaptic components decreased in AD patients while their RNA expression remained modest which indicates that post-transcriptional protein degradation plays a central role in AD pathogenesis. The fatty-acid oxidation pathway (Fig. 6c and 6g) contained 86 genes (Figure S10a & S10b) with only two overlapping genes (FABP3/5) that showed increased protein levels which indicate impaired lipid catabolism. The oxidative stress pathway (Fig. 6d and 6h) contained 13 genes (Figure S11a & S11b) with 6 overlapping genes that included antioxidant proteins PRDX6, and PSPC1 which showed increased protein levels with small changes in RNA expression.

The Gene Ontology enrichment results (Fig. 6j and 6l) confirmed these observations by showing that biological processes involved cytoplasmic translation and synaptic transmission and molecular functions included ribosomal components and rRNA binding and synaptic regulators such as glutamate receptor binding and cellular components showed dominance of ribosomes and postsynaptic density and mitochondrial inner membrane complexes. The KEGG pathway (Fig. 6m) and WikiPathways (Fig. 6n) analysis confirmed that ribosome and oxidative phosphorylation pathways dominate the data set together with MAPK, calcium and GPCR signaling pathways. The network analysis (Fig. 6o) grouped the results into three main clusters which included ribosomal proteins and synaptic dysfunction and mitochondrial and oxidative phosphorylation pathways. ATP5O and ATP5A1 act as a bridge between the ribosomal hub and synaptic nodes.The pathophysiology of AD results from increased ribosome/mRNA processing activity together with reduced neuronal signaling and disrupted mitochondrial and synaptic and metabolic and oxidative stress pathways. The two approaches show limited shared elements, yet their results demonstrate that ribosomal activity and synaptic dysfunction and mitochondrial damage work together to drive neurodegenerative processes.

Lipidomic analysis

To understand the lipidomic changes associated with AD, we performed untargeted lipidomics of cortex samples obtained from AD and control groups (Figure S12a). The lipidomic profiling identified several phospholipids and lipid mediators species changed in AD. Analysis via PLS-DA scatterplots (Fig. 7a) demonstrated clear cluster of

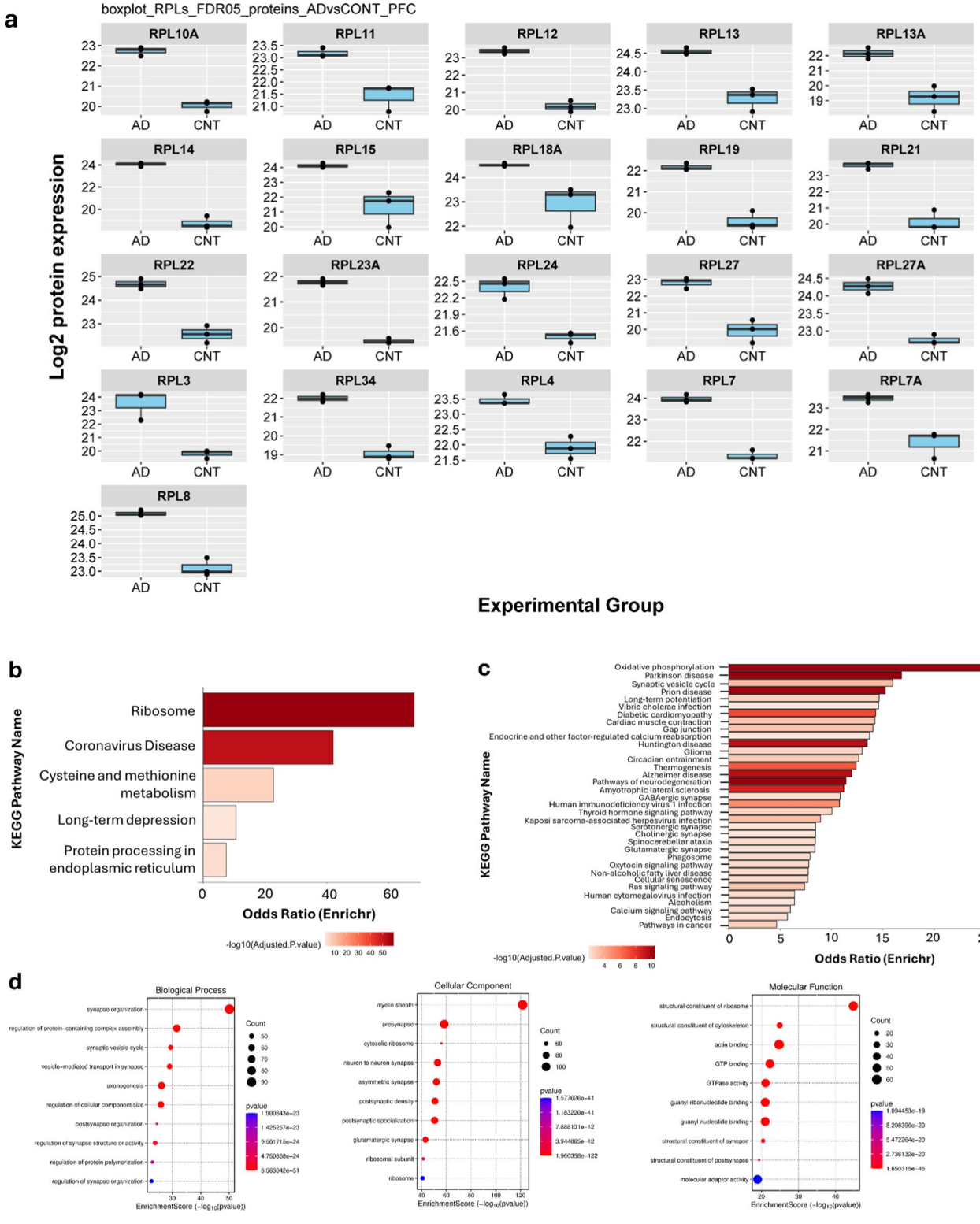

Fig. 5 **a** Boxplots for different ribosomal protein L isoforms (RPLs) with FDR ≤ 0.05. Enrichr analysis for overrepresentation of KEGG pathways among differentially expressed proteins (FDR ≤ 0.01) for **b** upregulated and **c** downregulated proteins respectively in AD. **d** Enrichment bubble plot for biological process, cellular component, and molecular function. **e** Circos plot for different pathways

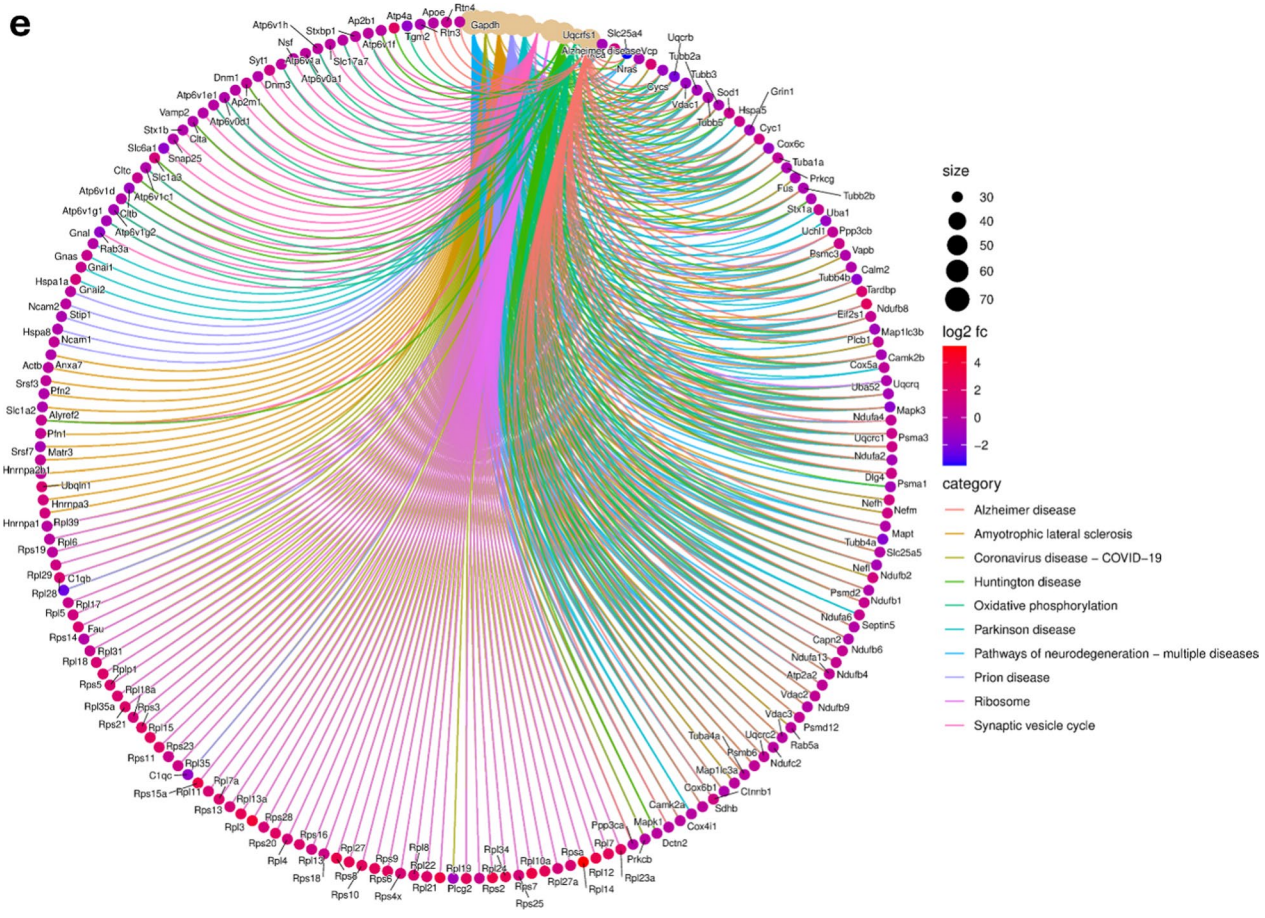

Fig. 5 (continued)

the AD and control samples based on the lipid profiles. The variable importance plots (VIP) (Fig. 7b) identified phospholipids species such PG, PI, PS, PC, PE as important contributor to the clustering of the groups. Notably, changes in in phospholipid metabolism are known to modulate mitochondrial function and create oxidative stress in various neurodegenerative diseases [59, 60]. Further, heatmap (Fig. 7c) shows the expression of the differentially expressed ($p \leq 0.05$) phospholipids and show an enrichment of very long chain PG moieties carbon chain > 24 (VLC-PG), suggesting effects on membrane stability and rigidity. Additionally, the known structural role of PG in mitochondrial membrane structure [61] and inflammation suggests that alterations in VLC-PGs can potentially influence mitochondrial dysfunction and chronic inflammation in AD, similar to what has been reported for frontotemporal dementia [62]. Furthermore, from the boxplots depicting the expression distribution of the top 7 most significantly regulated phospholipids (based on FDR ≤ 0.05) (Fig. 7d), there are evident changes in the levels of various lipid species. The levels of PG (28:8), PG (37:3), PG (40:6), and PI (42:10) were significantly increases in the AD samples. This dysregulation in the phospholipids might affect the mitochondrial membrane composition and increase the oxidative damage, in line with the evidence of lipid homeostasis being disturbed in the pathogenesis of AD [63]. However, PG (37:6) and PS (40:7) were significantly decreased in the AD group compared to the controls. PC species were mainly upregulated in AD, whereas PA and PS species were downregulated in AD (Fig. 7c). PE species with very long carbon chains (> 30) were downregulated in AD, whereas moderately long-chain PE species (< 30) were upregulated in AD.

Lipidomic profiling of phospholipids by acyl chain length revealed unique variations between different classes of phospholipids in the AD vs. control groups. The upregulation of very large chain carbons (C32–C44)-PC species suggests enhanced membrane turnover. The downregulation of PA and PS species points to impaired lipid biosynthesis and apoptotic signaling pathways. The downregulation of PE species indicates mitochondrial membrane instability. The observed changes in Fig. 7e indicate that AD pathology results from extensive membrane reorganization and lipid regulatory disturbances [64, 65].

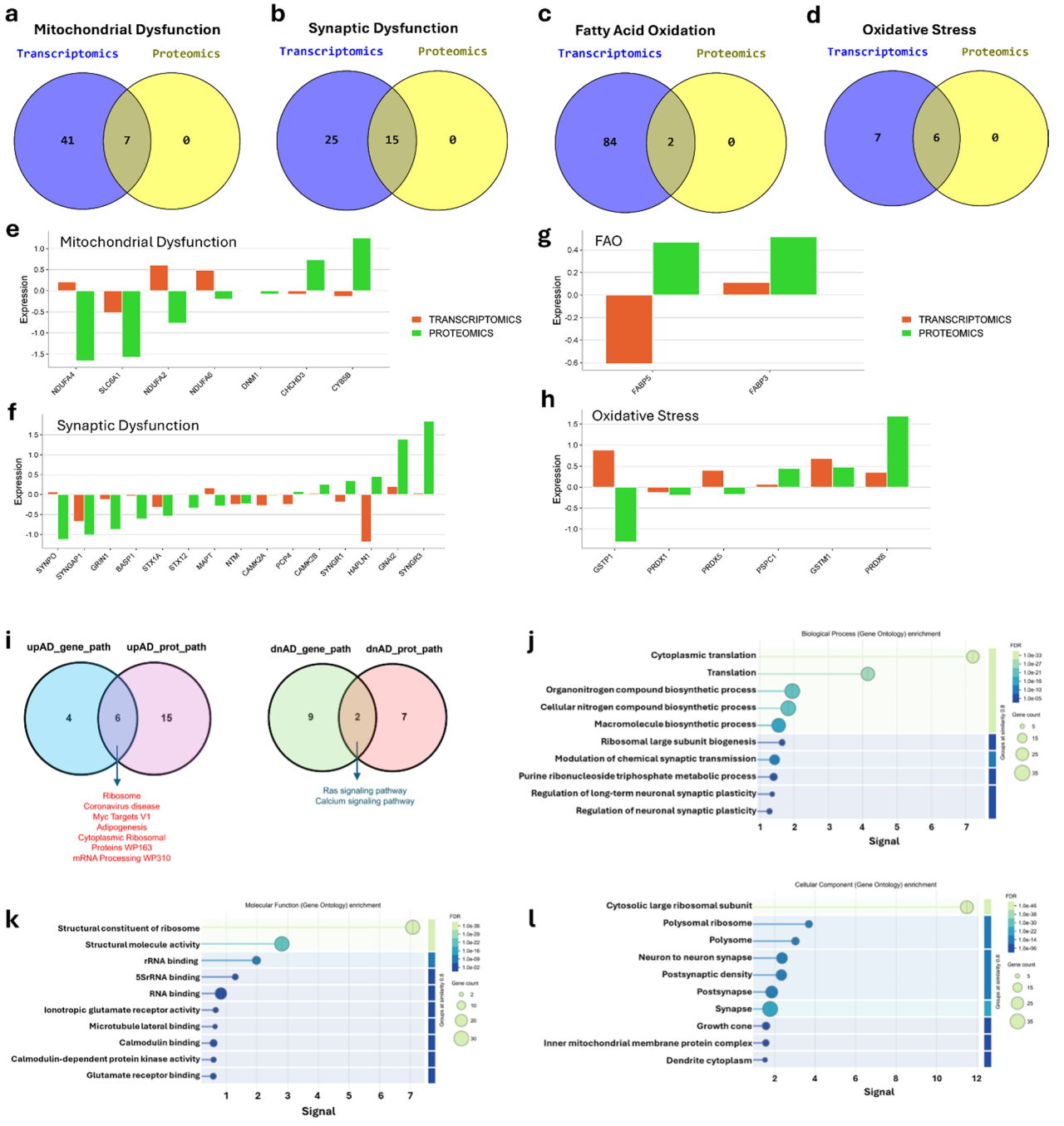

Fig. 6 Venn diagram shows the overlap between the transcriptomics (blue) and proteomics (light blue) for four families, namely **a** Mitochondrial dysfunction, **b** Synaptic dysfunction, **c** Fatty Acid Oxidation and **d** Oxidative stress. **e**-**h** Bar plots show the common genes across the listed transcriptomics (orange) and proteomics (green) pathways, with changes in gene and protein expression indicated by log_2Fold Change. **i** Venn analysis of the enriched pathways in transcriptome and proteome in the cortex showing common upregulated and downregulated pathways in AD. **j**-**l** demonstrates the GO enrichment analysis- **j** Biological Process, **k** Molecular function and **l** Cellular Component. **m**, **n** show the KEGG pathway and the WikiPathways, respectively. X-axis = enrichment signal; bubble size = gene count; bubble color = FDR (darker = more significant); right bars show cluster similarity. **o** String PPI network shows three modules: Dense ribosomal hub, oxidative and mitochondrial clusters along with the synaptic module

In order to investigate the formation of bioactive lipids, we also performed targeted analysis of lipid mediators (Figure S12b). The PCA plot (Fig. 7f) showed a distinct cluster of AD & control samples, indicating that the lipid mediator profiles are different in those two groups. We observed decrease of DHSM (13:3, 12:1, 13:1). Leukotriene E4, Nitro fatty acid($OA(NO_2)_2NO$), HerCer (14:1), and DAG (27:6) in AD. Surprisingly, Oxylipin (5,6 DHET) was upregulated in AD compared to the controls (Fig. 7g).

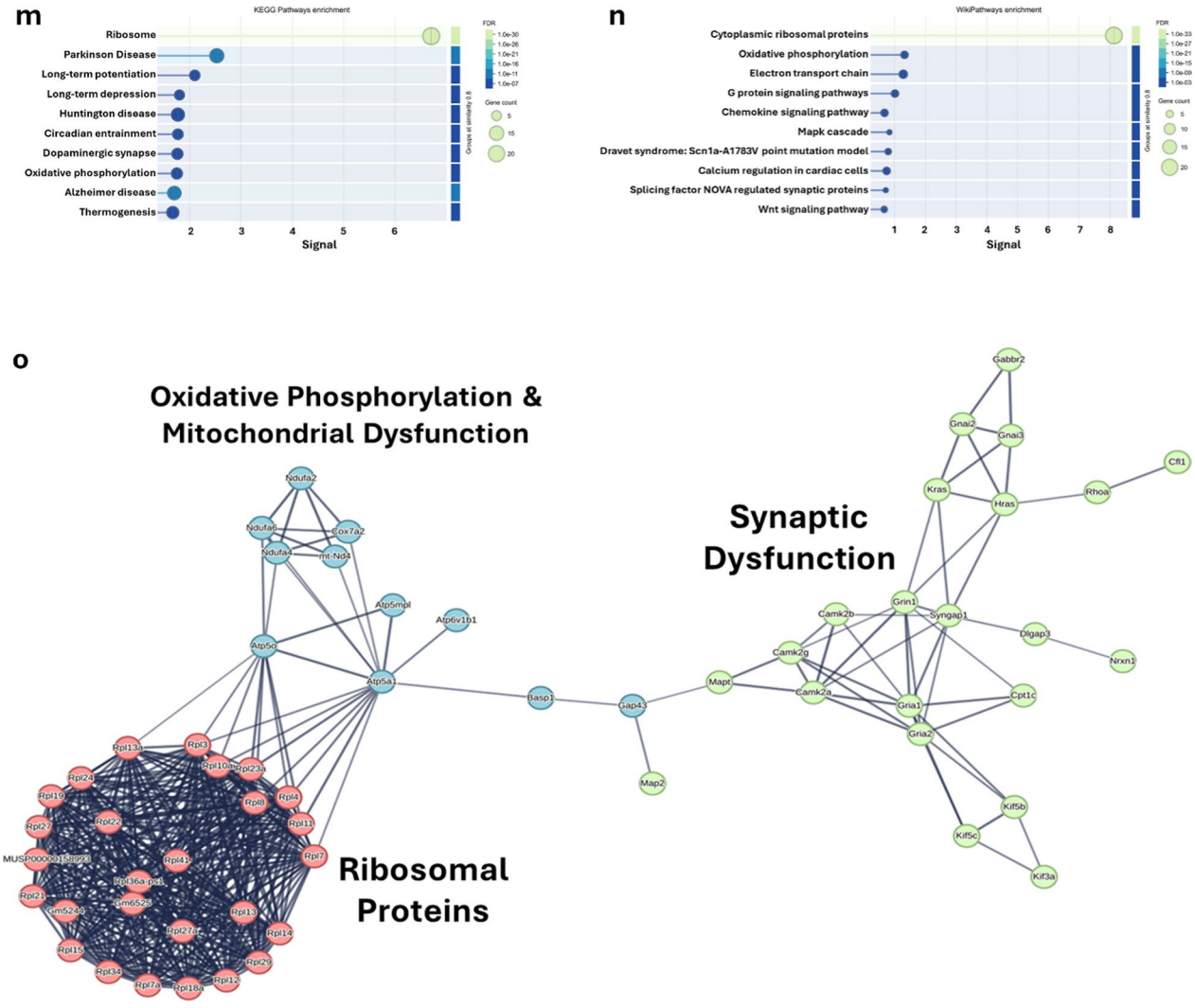

Fig. 6 (continued)

Integration of lipidomics with transcriptomic and proteomic data reveals a coordinated membrane remodeling program in AD cortex. Lipidomic profiling demonstrates marked heterogeneity within phospholipid classes, including dramatic accumulation of select phosphatidylglycerol (PG) species alongside depletion of others, consistent with disrupted mitochondrial membrane organization and cardiolipin remodeling. We observed PG species were strongly upregulated (e.g., PG (40:6) ~ 52×, PG (45:5) ~ 97×, PG (37:3) ~ 55×), while some PG species were strongly downregulated (e.g., PG (37:6) ~ 0.04×, PG (48:7) ~ 0.10×). Accumulation of select PG species reflects mitochondrial membrane remodeling and impaired CL maturation (Fig. 8a and b). This aligns with reduced mitochondrial biogenesis and structural support (Ppargc1a↓, Opa1/Tfam/Mfn2↓, VDAC1 protein↓) and activation of mitochondrial stress responses. The network analysis of lipidomics data (Fig. 8c) showed the significant activation ($p < 0.001$) of PS to PE conversion pathway. The canonical synthesis pathway showed that Ptdss1 is responsible for the conversion of PC to PS, and Ptdss2 is responsible for the conversion of PE to PS in the ER (Fig. 8e) [66]. The enzyme PSD is responsible for the conversion of PS to PE in the mitochondria (Fig. 8e). Our RNA-seq data for the cortex region showed upregulation of Psd and downregulation of Ptdss1 and Ptdss2 (Fig. 8f). This is reflected in our lipidomics dataset, where PS is significantly downregulated ($p < 0.01$) in AD compared to the control brain (Fig. 8d). PG is the direct biosynthetic precursor of cardiolipin (CL) and is enriched in mitochondrial membranes. The dramatic increase in specific polyunsaturated PG species suggests disrupted cardiolipin remodeling. The RNA-seq data showed upregulation of genes associated with CL biosynthesis (Fig. 8k).

Our lipidomic dataset showed widespread increase of PC species, particularly long-chain and saturated species (e.g., PC (35:0), PC (34:0), PC (30:0), PC (36:0), and PC (41:9)). PC is the dominant structural lipid of the ER and

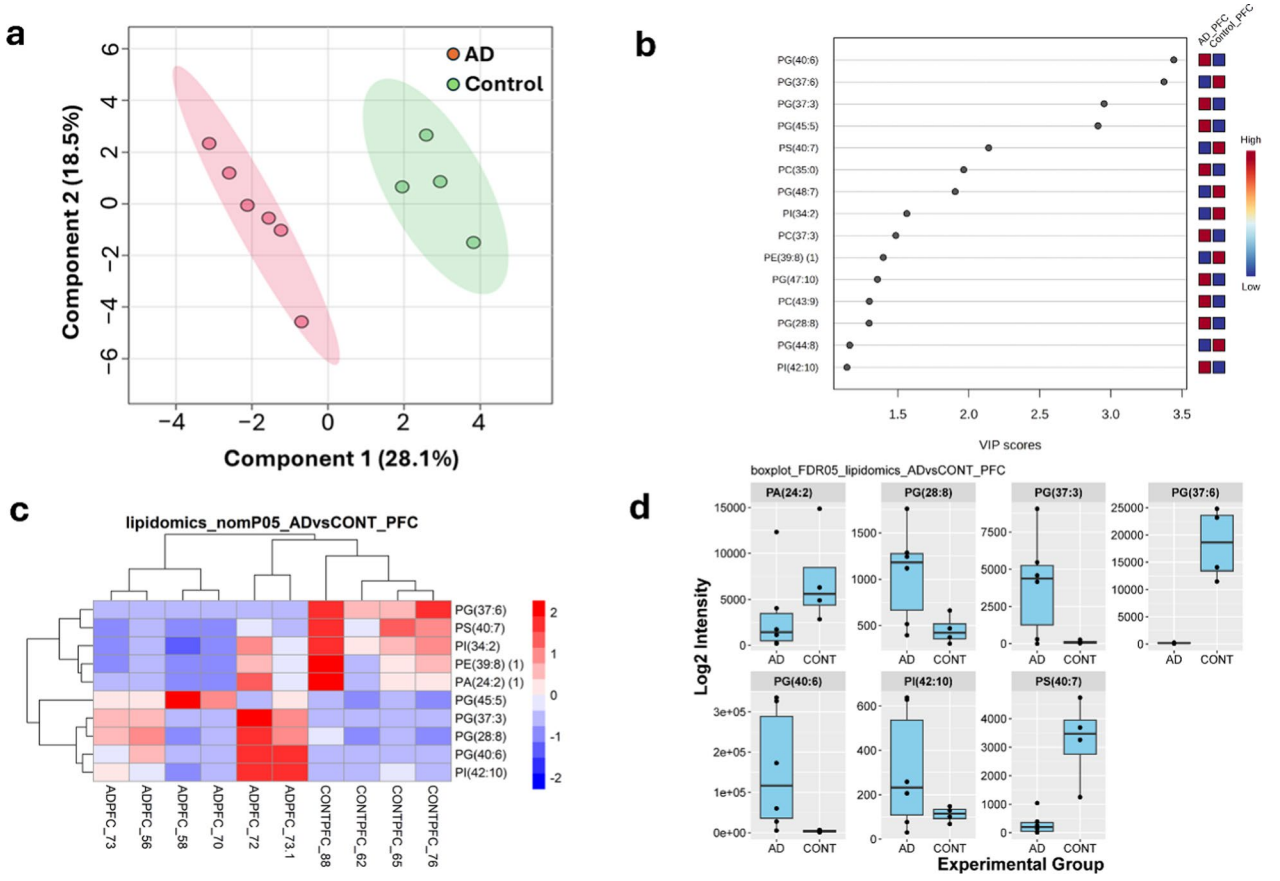

Fig. 7 Lipidomic analysis comparing the lipidome in the cortex of AD and control samples. **a** PLS-DA scatterplot showing the distinct cluster for AD and control **b** PLS-DA based VIP plot showing top 15 lipid features for discriminating AD from control samples, **c** Heatmap showing the significantly differentially expressed lipids in AD vs. control, cortex ($p \leq 0.05$) **d** Boxplots for top the 7 most differentially expressed lipids in the cortex (based on FDR ≤ 0.05), **e** Plot showing the variation in the carbon chain length with $\log_2$FC (AD vs. control) for the most significant lipids with FDR ≤ 0.05 **f** PLS-DA scatterplot showing the cluster for AD and control samples based on lipid mediators. **g** PLS-DA-based VIP plot showing the top 15 lipid mediator features for distinguishing AD from control samples. Expression levels are row-normalized and color-coded from blue (low expression) to red (high expression)

rough ER, where ribosomes dock [67]. This aligns with the upregulation of ribosomal proteins in the proteomics data (2–15×) as well as upregulation of ER stress sensors and ER chaperones such as HSPA5 and HSP90B1 (Fig. 8m). HSPA5 (BiP/GRP78) and HSP90B1 (GP96/GRP94) are critical endoplasmic reticulum (ER) chaperones that maintain protein homeostasis. Under normal conditions, HSPA5 binds to ER transmembrane sensors (PERK, IRE1, ATF6), keeping them inactive. When unfolded proteins accumulate, HSPA5 releases these sensors, triggering the unfolded protein response (UPR) to alleviate stress [68]. Similarly, HSP90B1 is a member of the HSP90 family and is critical for folding specialized proteins in the secretory pathway, particularly Toll-like receptors (TLRs) and integrins [69]. Figure 8m also showed upregulation of ribosome biogenesis-related protein NCL in our proteomics data.

The opposing regulation of mitochondrial inner and outer membrane proteins in AD cortex (Fig. 8i) reveals a compartment-specific stress adaptation rather than uniform mitochondrial loss. Upregulation of inner mitochondrial membrane and cristae-organizing proteins (IMMT, CHCHD3, PHB1) and metabolite transporters (SFXN1, SFXN3) (Fig. 8i) suggests an adaptive effort to stabilize inner membrane architecture, preserve respiratory complex organization, and support mitochondrial proteostasis in the setting of membrane lipid remodeling. In contrast, downregulation of outer mitochondrial membrane components involved in protein import and metabolite exchange (TOMM70 and VDAC1/2/3) (Fig. 8i) indicates reduced mitochondrial throughput and functional isolation under chronic stress. This inner-membrane-protective and outer-membrane-restrictive configuration is consistent with mitonuclear–proteostatic imbalance, in which increased nuclear translation and ribosome abundance outpace mitochondrial import and handling capacity, thereby engaging UPR^{mt} and ISR pathways observed in the AD dataset.

We observed reduced polyunsaturated PE species, although overall PE reduction in AD was not significant

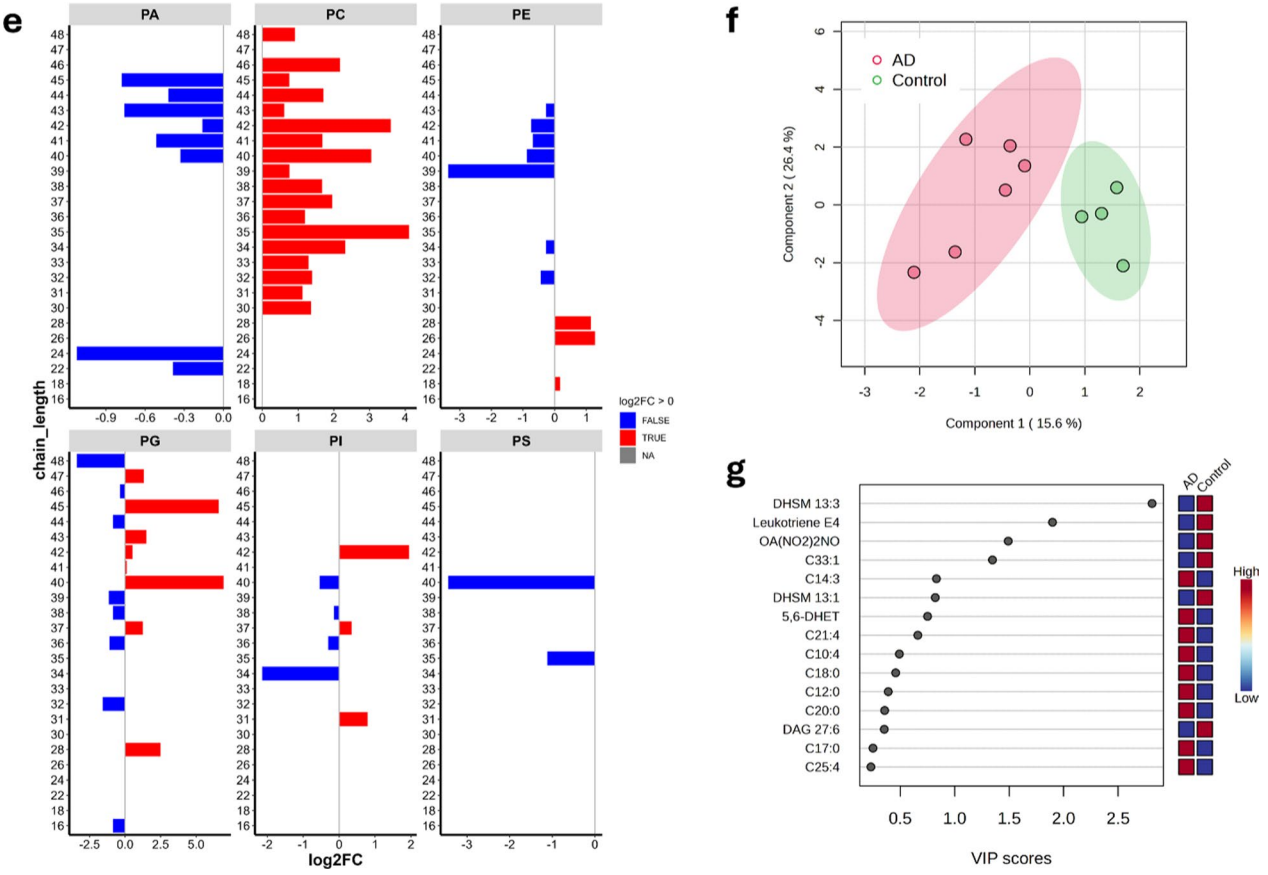

Fig. 7 (continued)

(Fig. 8b and 8d). Broad depletion of PUFA-PE leads to mitochondrial membrane instability and impaired mitophagy efficiency [70]. This also activates UPR^{mt} and ISR. Together, these data support a model in which lipid remodeling underlies stress-adaptive translational reprogramming and proteostasis in the AD brain, particularly within reactive glial populations, despite compromised mitochondrial metabolic efficiency. Further, the functional network analysis (Fig. 8h) of the lipidomic data showed enrichment clusters for glycerophospholipid and sphingolipid metabolism. Functional networks generally reveal which lipids act together as part of a coordinated biological response.

Discussion

Our multi-omics analysis of cortex tissue from 5xFAD Alzheimer's disease (AD) mice (age = 17 months) revealed complex yet convergent molecular signatures that implicate dysregulation of ribosomal biogenesis, protein homeostasis, vesicular trafficking, and lipid metabolism at an advanced stage AD pathogenesis to understand the terminal proteostatic collapse of the Alzheimer's brain, a stage characterized by significant neuronal loss and maximum amyloid-beta accumulation that is not fully realized in younger cohorts. Current study provides a comprehensive view of the ribosomal complex, showing coordinated upregulation of both the 60 S and 40 S subunits (Figure S13). This indicates a late-stage drive toward increased ribosomal abundance, likely mediated by the Integrated Stress Response (ISR) and UPR^{mt} (mitochondrial unfolded protein response) (Figure S14) as an attempt to maintain cellular homeostasis despite severe bioenergetic failure. Across both RNA-seq and proteomics datasets, we observed a consistent upregulation of multiple ribosomal proteins (RPL3, RPL4, RPL7, RPL8 RPL10A, RPL11, RPL12, RPL13, RPL13A, RPL14, RPL15, RPL18A, RPL19, RPL21, RPL22, RPL23A, RPL24, RPL27, RPL27A, RPL34) except RPL29 and the translation elongation factor EEF1G. This coordinated increase suggests an expansion of ribosomal capacity and translational activity, potentially reflecting reactive gliosis or stress-adaptive translational reprogramming in the AD brain. Prior studies have reported similar ribosomal protein upregulation in both human AD cortex and murine models, interpreted as a compensatory response to protein misfolding and oxidative stress [71, 72]. The concomitant elevation of SOD1 further supports an

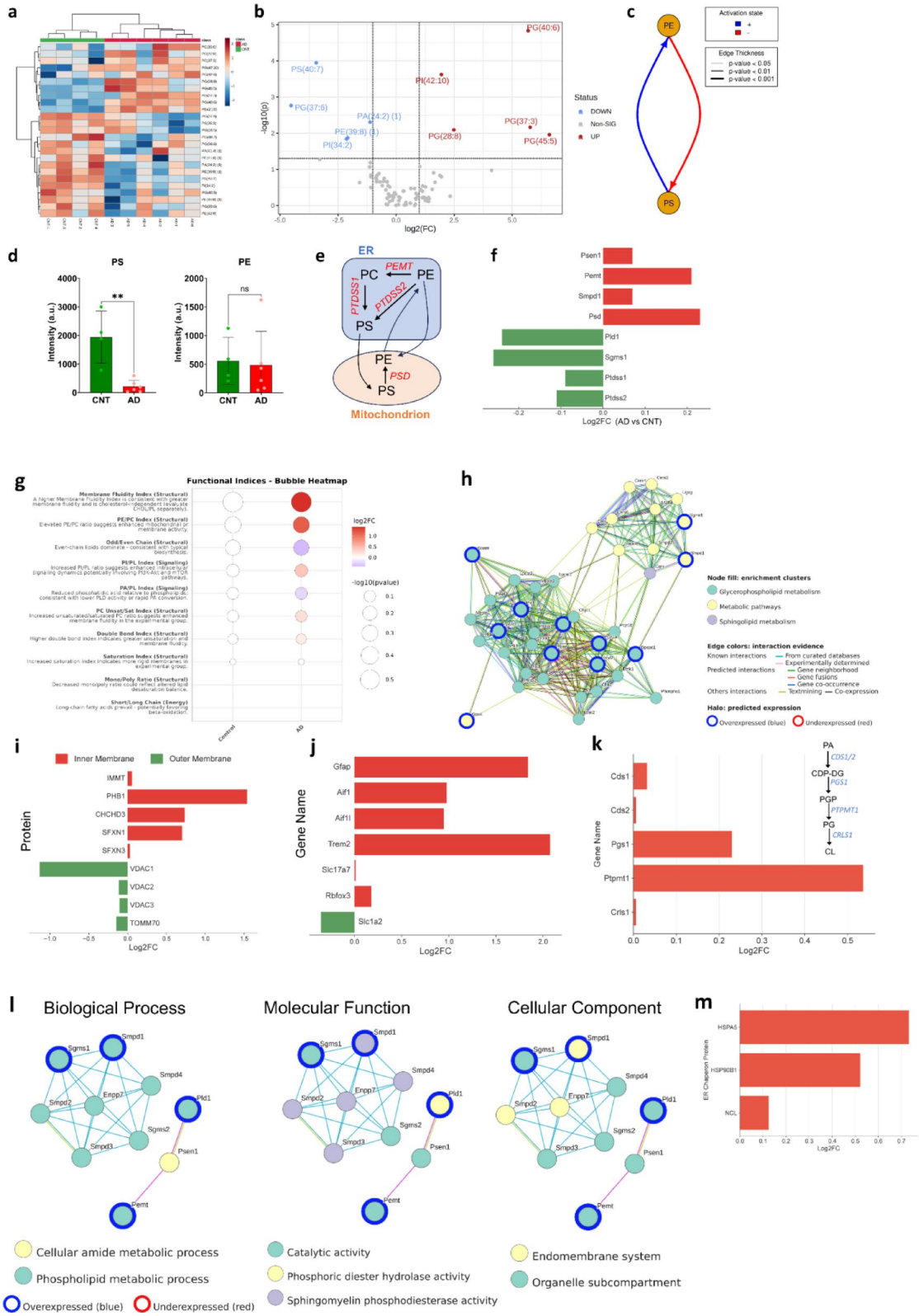

Fig. 8 (See legend on next page.)

(See figure on previous page.)

Fig. 8 Integrated multi-omics analysis reveals coordinated membrane and organelle stress responses in the Alzheimer's disease (AD) cortex. **a** Heatmap showing differential lipid species expression across AD and control samples. **b** Volcano plot highlighting significantly upregulated and downregulated phospholipid species in AD compared with controls. **c** Network diagram illustrating interactions between phosphatidylethanolamine (PE) and phosphatidylserine (PS) species; edge thickness reflects the strength of disease-associated modulation ($p < 0.05$ to 0.001). **d** Bar graphs depicting mean total PS and PE levels in control and AD samples; PS is significantly reduced in AD ($p < 0.01$), while PE does not reach statistical significance. **e** Schematic of canonical phospholipid synthesis pathways involving key enzymes PTDSS1, PTDSS2, PEMT, and PSD, highlighting endoplasmic reticulum (ER)–mitochondria crosstalk. **f** Bar plot showing $\log_2$ fold changes in mRNA expression of genes associated with the pathways shown in (**e**). **g** Functional indices bubble heatmap summarizing lipidomic indices comparing AD and control samples; bubble size and color intensity represent statistical significance and magnitude of change, respectively. **h** Functional lipidomic network illustrating enriched clusters related to glycerophospholipid metabolism, broader metabolic pathways, and sphingolipid metabolism; edges indicate interaction evidence, and blue halos denote predicted gene overexpression. **i** Bar graph of differentially expressed proteins (DEPs; $\log_2$ fold change) associated with mitochondrial function, showing upregulation of inner membrane proteins (red) and downregulation of outer membrane proteins (green). **j** Gene expression profiles of selected glial marker genes. **k** Differentially expressed genes ($\log_2$ fold change) for cardiolipin (CL) synthesis pathway. **l** Networks of biological processes, molecular functions, and cellular components involving sphingolipid and phospholipid metabolism genes; **m** Differential expression of genes associated with ER stress ($\log_2$ fold change)

oxidative stress–driven ribosomal remodeling, consistent with mitochondrial dysfunction in AD [73].

Notably, TNK2 (ACK1) and ATP6V1G1 displayed discordant regulation between RNA and protein levels—upregulated in RNA-seq yet downregulated in proteomics. Such mRNA–protein mismatches are increasingly recognized in neurodegeneration [74], often arising from post-transcriptional suppression, translational inefficiency (e.g., via eIF2α phosphorylation), or accelerated protein turnover. For TNK2, reduced protein abundance may impair receptor trafficking and synaptic signaling, while ATP6V1G1 loss could compromise lysosomal acidification and autophagic clearance [75–77] both processes central to amyloid and tau pathology [78], although direct association of TNK2 with AD has not been shown before [79, 80]. These findings suggest a failure of transcriptional compensation to restore protein function, possibly reflecting persistent translational stress in AD neurons.

Our integrated Transcriptomics and proteomics analysis of AD demonstrates the ribosomal overactivity which leads to the mitochondrial dysfunction and synaptic network breakdown. Along with the persistent increase of ribosome and mRNA processing pathways indicates abnormal translational control mechanisms which research has shown to occur in AD and other neurodegenerative diseases [81], the downregulation of Ras and calcium signaling pathways together with synaptic proteins namely SYNGAP1, SYNPO, GRIN1, CAMPK2A, MAPT and STX12/A and modest RNA changes underscores the role of the post-translational protein degradation in the synaptic failure [82]. The observed decrease (NDUFA2/4/6) and increase (CHCHD3 and CYB5B) in oxidative phosphorylation proteins with partial transcriptional adaptation confirms the established relationship between mitochondrial dysfunction and Alzheimer's disease progression [83]. The elevated levels of antioxidant proteins PRDX6 and GSTM1 demonstrate stress response mechanisms that match findings from previous proteomic investigations [84]. The elevation of fatty acid oxidation proteins FABP3/5 supports the theory that lipid metabolic problems make neurons more susceptible to damage [85]. Network analysis revealed that ribosomal hubs and synaptic components and mitochondrial complexes formed connected clusters through ATP5O and ATP5A1 which supports the theory that protein synthesis dysregulation and energy failure and synaptic deterioration work together to cause AD pathogenesis.

Protein synthesis is energetically demanding. In the Alzheimer's disease brain, ribosome biogenesis represents a strategic investment of cellular energy rather than an indication of unrestricted anabolic growth. Disease pathology is characterized by elevated protein turnover driven by the accumulation of misfolded proteins, synaptic damage, and chronic inflammatory signaling. As a result, immune mediators, stress-response proteins, and secreted factors must be continuously synthesized, while damaged or dysfunctional proteins require constant replacement to preserve cellular viability. Under these conditions, cells prioritize energy allocation toward maintaining translational capacity, proteostasis, and stress-adaptive responses, even when mitochondrial metabolic efficiency is compromised. This redistribution of energetic resources supports short-term survival and functional resilience in a hostile pathological environment, rather than long-term metabolic efficiency or growth, and provides a mechanistic rationale for increased ribosomal protein expression in the AD cortex (Figure S15).

Lipidomic profiling revealed a broad downregulation of bioactive lipid mediators, including dihydrosphingomyelin (DHSM 13:3, 12:1, 13:1), leukotriene E4, nitro fatty acids, hexosylceramide (HexCerd 14:1), and diacylglycerol (DAG 27:6). Sphingolipid depletion has been linked to disrupted membrane microdomains and impaired synaptic vesicle fusion in AD [86], while reduced leukotrienes and nitro fatty acids may indicate altered neuroinflammatory signaling and redox balance [87, 88]. In contrast, 5,6-dihydroxyeicosatrienoic acid (5,6-DHET) was elevated, potentially reflecting increased soluble epoxide hydrolase activity, which has been implicated in neuroinflammation and vascular dysfunction in AD

models [89–91]. At the glycerophospholipid level, we observed upregulation of phosphatidylglycerol (PG) species alongside downregulation of phosphatidylserine (PS), phosphatidylinositol (PI), and phosphatidylethanolamine (PE), consistent with previous reports of altered membrane lipid composition and impaired phospholipid metabolism in AD [92, 93].

Functional network analysis of lipidome further demonstrates the lipid remodeling in AD cortex which is highly coordinated, with enrichment of glycerophospholipid and sphingolipid metabolic modules [94]. This network level coordination likely adapts cell membranes metabolic rewiring under proteotoxic and mitochondrial stress [95]. Glycerophospholipids define membrane structure, curvature and organelle identity, their changes are linked to mitochondrial activity and endoplasmic reticulum function [96]. Meanwhile, shifts in sphingolipids influence membrane microdomains while also sensing cellular stress [97]. In AD, significant shifts in PS and PE are associated with ER stress, mitochondrial dysfunction, and modulation of specific proteins [98].

Conclusions

We performed a multiomics study combining transcriptomics, proteomics, and lipidomics using the cortex region of the 5xFAD and control mice. Our integrated results from these studies suggest a coordinated disruption of the translational machinery, vesicular trafficking, lysosomal function, and membrane lipid composition in the AD cortex. The widespread ribosomal protein upregulation suggests an attempt to enhance translational capacity under proteostatic stress, yet selective deficits in key trafficking and degradation proteins, coupled with lipid remodeling, may undermine neuronal and glial capacity to maintain synaptic and metabolic homeostasis. The concordance for ribosomal protein changes in RNA-seq and proteomics data, along with the RNA–protein discordance for TNK2 and ATP6V1G1, and the lipid mediator shifts, underscores the necessity of multiomics approaches to fully capture the complexity of AD pathobiology. Future work will investigate the cell-type specificity of these alterations and determine whether the observed lipidomic changes drive or result from the proteomic and transcriptomic reprogramming in AD.

Supplementary Information

The online version contains supplementary material available at https://doi.org/10.1186/s40478-026-02254-6.

Supplementary Material 1

Supplementary Material 2

Supplementary Material 3

Supplementary Material 4

Supplementary Material 5

Acknowledgements

This project utilized the Cell Biology and Bioimaging Core that is supported in part by COBRE (P20 GM135002 & P20 GM103528) and NORC (P30 DK072476) center grants from the National Institutes of Health.

Author contributions

Conceptualization: Manas Ranjan Gartia. Methodology: Kirti Agrawal, Blessing C. Egbejiogu, Alex Walls, Katarina Jones, Sujoy Ghosh; writing—original draft preparation: Kirti Agrawal, Sujoy Ghosh, Blessing C. Egbejiogu, Alex Walls, Manas Ranjan Gartia ; writing—review and editing: Kirti Agrawal, Blessing C Egbejiogu, Tolulope Adeyelu, David Burk, Kermit K Murray, Alex Walls, Katarina Jones, Shawn Campagna, Joseph Francis, Sujoy Ghosh, Olalekan M Ogundele, and Manas Ranjan Gartia; funding acquisition: Manas Ranjan Gartia; resources: Manas Ranjan Gartia, David Burk, Kermit K Murray, Shawn Campagna, Joseph Francis, Sujoy Ghosh, Olalekan M Ogundele; supervision: Manas Ranjan Gartia.

Funding

Research reported in this publication was supported by the National Institute of General Medical Sciences of the National Institutes of Health under award number R35GM150564. M.R.G. was supported by the National Science Foundation (NSF CAREER award number: 2045640).

Data availability

All the data and materials supporting the conclusions of this article are included in this article. The RNAseq data is available on the Gene Expression Omnibus (GEO) database with the accession number: **GSE316829**. The proteomics and lipidomic data are attached as an Proteomics_AD.csv and lipidome_AD.xlsx file as Supplementary Information, respectively.

Declarations

Ethics approval and consent to participate

The animal studies were in accordance with the Institutional Animal Care and Use Committee (IACUCAM-20-093) at LSU.

Conflict of interest

The authors declare no conflict of interest.

Received: 18 October 2025 / Accepted: 6 February 2026
Published online: 23 February 2026

References

1. Rayathala J, Kumar K (2022) Review on alzheimer's disease: Past, present and future. J Innovations Appl Pharm Sci (JIAPS), 28–31
2. Magalingam KB, Radhakrishnan A, Ping NS (2018) & Haleagrahara, N. Current concepts of neurodegenerative mechanisms in Alzheimer's disease. *BioMed research international* 3740461 (2018)
3. Sohrabi HR, Weinborn M (2019) Cognitive impairments in Alzheimer's disease and other neurodegenerative diseases. Neurodegeneration Alzheimer's Disease: Role Diabetes Genet Horm Lifestyle, 267–290
4. Yiannopoulou KG, Papageorgiou SG (2020) Current and future treatments in alzheimer disease: an update. J Cent Nerv Syst Dis 12:1179573520907397. https://doi.org/10.1177/1179573520907397
5. Hardy J (2002) D. S. The amyloid hypothesis of Alzheimer's disease: progress and problems on the road to therapeutics. Science
6. Serrano-Pozo A, Masliah MFE, Hyman BT (2011) Neuropathological alterations in Alzheimer disease. *Cold Spring Harbor perspectives in medicine*
7. Bloom GS (2014) Amyloid-β and tau: the trigger and bullet in alzheimer's disease pathogenesis. LAMA Neurol
8. Nussbacher JK, Lagier-Tourenne RBC, Yeo GW (2015) RNA-binding proteins in neurodegeneration: seq and you shall receive. Trends Neurosci
9. Magadi SS et al (2025) Alternative splicing generates a Ribosomal Protein S24 isoform induced by neuroinflammation and neurodegeneration. *bioRxiv*, 2025.2003.2028.645676 https://doi.org/10.1101/2025.03.28.645676
10. Fusco CM et al (2021) Neuronal ribosomes exhibit dynamic and context-dependent exchange of ribosomal proteins. Nat Commun 12:6127
11. Sakers K et al (2017) Astrocytes locally translate transcripts in their peripheral processes. Proc Natl Acad Sci 114:E3830–E3838

12. Sapkota D et al (2022) Activity-dependent translation dynamically alters the proteome of the perisynaptic astrocyte process. Cell Rep 41
13. Vasek MJ et al (2023) Local translation in microglial processes is required for efficient phagocytosis. Nat Neurosci 26:1185–1195
14. Zhou X, Liao W-J, Liao J-M, Liao P, Lu H (2015) Ribosomal proteins: functions beyond the ribosome. J Mol Cell Biol 7:92–104. https://doi.org/10.1093/jmcb/mjv014
15. Warner JR, McIntosh KB (2009) How common are extraribosomal functions of ribosomal proteins? Mol Cell 34:3–11. https://doi.org/https://doi.org/ https://doi.org/10.1016/j.molcel.2009.03.006
16. Kapur M, Monaghan CE, Ackerman SL (2017) Regulation of mRNA translation in Neurons—A matter of life and death. Neuron 96:616–637. https://doi.org/https://doi.org/ https://doi.org/10.1016/j.neuron.2017.09.057
17. Boisvert F-M, van Koningsbruggen S, Navascués J, Lamond A (2007) I. The multifunctional nucleolus. Nat Rev Mol Cell Biol 8:574–585. https://doi.org/10.1038/nrm2184
18. Yamakawa A et al (2025) Alzheimer's disease May develop from changes in the immune system, cell cycle, and protein processing following alterations in ribosome function. Sci Rep 15:3838. https://doi.org/10.1038/s41598-025-88526-y
19. Lauretti E, Dabrowski K, Praticò D (2021) The neurobiology of non-coding RNAs and alzheimer's disease pathogenesis: Pathways, mechanisms and translational opportunities. Ageing Res Rev 71:101425. https://doi.org/10.1016/j.arr.2021.101425
20. Wolozin B (ed) (2014) D. A. (ed GeNeDis)
21. Martín V, Santpere NFG, Puig B, Marín R, Ferrer I, Díaz M (2010) Lipid alterations in lipid rafts from Alzheimer's disease human brain cortex. J Alzheimers Dis
22. Walter J (2013) G. v. E.-D. Cross-talk of membrane lipids and Alzheimer-related proteins. *Molecular neurodegeneration*
23. Hetman M, Slomnicki LP (2019) Ribosomal biogenesis as an emerging target of neurodevelopmental pathologies. J Neurochem 148:325–347. https://doi.org/10.1111/jnc.14576
24. Masi M et al (2022) Proteostasis Deregulation in Neurodegeneration and Its Link with Stress Granules: Focus on the Scaffold and Ribosomal Protein RACK1. *Cells* 11, 2590
25. Kudla G, Tollervey AMD, Plotkin JB (2009) Coding-Sequence Determinants of Gene Expression in Escherichia coli. *science* 324 https://doi.org/10.1126/science.1170160
26. Pechmann S (2013) Evolutionary conservation of codon optimality reveals hidden signatures of cotranslational folding. Nat Struct Mol Biol 20. https://doi.org/10.1038/nsmb.2466
27. Yu CH, Zhou YDZ, Wu C, Zhao F, Sachs MS, Liu Y (2015) Codon usage influences the local rate of translation elongation to regulate co-translational protein folding. Mol Cell 59. https://doi.org/10.1016/j.molcel.2015.07.018
28. Choe YJ, Hassemer SPT, Körner R, Vincenz-Donnelly L, Hayer-Hartl M, Hartl FU (2016) Failure of RQC machinery causes protein aggregation and proteotoxic stress. Nature 531. https://doi.org/10.1038/nature16973
29. Buhr F, Thommen SJM, Mittelstaet J, Kutz F, Schwalbe H, Rodnina MV, Komar AA (2016) Synonymous codons direct cotranslational folding toward different protein conformations. Mol Cell 61. https://doi.org/10.1016/j.molcel.2016.01.008
30. Wu CCC, Zinshteyn APB, Regot S, Green R (2020) Ribosome collisions trigger general stress responses to regulate cell fate. Cell 182. https://doi.org/https://doi.org/ https://doi.org/10.1016/j.cell.2020.06.006
31. Ubaida-Mohien C et al (2019) Discovery proteomics in aging human skeletal muscle finds change in spliceosome, immunity, proteostasis and mitochondria. Elife 8:e49874
32. Anisimova AS et al (2020) Multifaceted deregulation of gene expression and protein synthesis with age. *Proceedings of the National Academy of Sciences* 117, 15581–15590
33. Feng LW, Song G, Feng Q, Su X, Ji J, Li G (2023) Proteomics revealed an association between ribosome-associated proteins and amyloid beta deposition in alzheimer's disease. Metab Brain Dis 38:29–45. https://doi.org/10.1007/s11011-023-01330-3
34. Li Y, Chen HYC, Li S, Zhang Z, Xu H, Zhu F, Liu J, Spencer PS, Dai Z, Yang X (2020) Proteomic profile of mouse brain aging contributions to mitochondrial dysfunction, DNA oxidative damage, loss of neurotrophic factor, and synaptic and ribosomal *Oxidative medicine and cellular longevity* https://doi.org/10.1155/2020/5408452
35. Song Z et al (2020) Comprehensive proteomic profiling of urinary exosomes and identification of potential non-invasive early biomarkers of alzheimer's disease in 5XFAD mouse model. Front Genet 11:565479
36. The Jackson Laboratory. B6.Cg-Tg(APPswe,PSEN1dE9)85Dbo/Mmjax (2021)
37. Song Z, Zhang YXL, Zhou L, Zhang Y, Han Y, Li X, Yu P, Qu Y, Zhao W, Qin C (2020) Comprehensive proteomic profiling of urinary exosomes and identification of potential non-invasive early biomarkers of Alzheimer's disease in 5XFAD mouse model. Front Genet 11. https://doi.org/10.3389/fgene.2020.565479
38. Jullienne A et al (2023) Cortical cerebrovascular and metabolic perturbations in the 5xFAD mouse model of alzheimer's disease. Front Aging Neurosci 15:1220036
39. Jullienne A, Szu JI, Quan R, Trinh MV, Norouzi T, Noarbe BP, Bedwell AA, Eldridge K, Persohn SC, Territo PR, Obenaus A (2023) Cortical cerebrovascular and metabolic perturbations in the 5xFAD mouse model of Alzheimer's disease. Cortical Cerebrovasc metabolic perturbations 5xFAD mouse model Alzheimer's disease 15. https://doi.org/10.3389/fnagi.2023.1220036
40. Kelley DP et al (2022) Pharmahuasca and DMT rescue ROS production and differentially expressed genes observed after predator and psychosocial stress: relevance to human PTSD. ACS Chem Neurosci 13:257–274
41. Dong C, Richardson LT, Solouki T, Murray KK (2022) Infrared laser ablation microsampling with a reflective objective. J Am Soc Mass Spectrom
42. Dong CD, Murray F (2022) K. K. Infrared laser ablation microsampling for small volume proteomics. J Am Soc Mass Spectrom
43. Mal M, A HILIC-Based SW (2011) UPLC-MS method for the separation of lipid classes from plasma. Waters Application Note
44. Clasquin MF, Rabinowitz EMJD (2012) LC-MS data processing with MAVEN: a metabolomic analysis and visualization engine. Curr Protocols Bioinf. https://doi.org/10.1002/0471250953.bi1411s37
45. Agrawal S, Sehgal SKR, George S, Gupta R, Poddar S, Jha A, Pathak S (2019) El-MAVEN: a fast, robust, and user-friendly mass spectrometry data processing engine for metabolomics. High-throughput Metabolomics
46. Li Chen WL, Wang L, Xing X, Chen Z, Xin Teng X, Zeng AD, Muscarella Y, Shen A, Cowan MR, McReynolds BJ, Kennedy AM, Lato SR, Campagna (2021) Mona Singh & Joshua D. Rabinowitz. Metabolite discovery through global annotation of untargeted metabolomics data. *nature*
47. Wang L, Wang S, Li W (2012) RSeQC: quality control of RNA-seq experiments. Bioinformatics 28:2184–2185. https://doi.org/10.1093/bioinformatics/bts356
48. Martin M (2011) Cutadapt removes adapter sequences from high-throughput sequencing reads. 2011 17:3. https://doi.org/10.14806/ej.17.1.200
49. Dobin A et al (2012) STAR: ultrafast universal RNA-seq aligner. Bioinformatics 29:15–21. https://doi.org/10.1093/bioinformatics/bts635
50. Liao Y, Smyth GK, Shi W (2019) The R package Rsubread is easier, faster, cheaper and better for alignment and quantification of RNA sequencing reads. Nucleic Acids Res 47:e47–e47. https://doi.org/10.1093/nar/gkz114
51. Chen Y, Chen L, Lun, Aaron TL, Baldoni PL, Smyth GK (2025) EdgeR v4: powerful differential analysis of sequencing data with expanded functionality and improved support for small counts and larger datasets. Nucleic Acids Res 53. https://doi.org/10.1093/nar/gkaf018
52. Ritchie ME et al (2015) Limma powers differential expression analyses for RNA-sequencing and microarray studies. Nucleic Acids Res 43:e47–e47. https://doi.org/10.1093/nar/gkv007
53. Korotkevich G et al (2021) Fast gene set enrichment analysis. BioRxiv 060012. https://doi.org/10.1101/060012
54. Liberzon A et al (2011) Molecular signatures database (MSigDB) 3.0. Bioinformatics 27:1739–1740. https://doi.org/10.1093/bioinformatics/btr260
55. Kuleshov MV et al (2016) Enrichr: a comprehensive gene set enrichment analysis web server 2016 update. Nucleic Acids Res 44:W90–W97. https://doi.org/10.1093/nar/gkw377
56. Pang Z et al (2024) MetaboAnalyst 6.0: towards a unified platform for metabolomics data processing, analysis and interpretation. Nucleic Acids Res 52:W398–W406. https://doi.org/10.1093/nar/gkae253
57. Anusree Saha SD, Moin M, Dutta M, Bakshi A, Madhav MS, Kirti PB (2017) Genome-Wide identification and comprehensive expression profiling of ribosomal protein small subunit (RPS) genes and their comparative analysis with the large subunit (RPL) genes in rice. Front Plant Sci 8. https://doi.org/10.3389/fpls.2017.01553
58. Tang D et al (2023) SRplot: A free online platform for data visualization and graphing. PLoS ONE 18:e0294236
59. Pavel Katsel CL, Haroutunian V (2007) Gene expression alterations in the sphingolipid metabolism pathways during progression of dementia and

Alzheimer's disease: a shift toward ceramide accumulation at the earliest recognizable stages of Alzheimer's disease? PLoS ONE
60. Marcus OW, Grimm JM, Heike S (2017) Grimm1 and Tobias Hartmann. APP function and lipids: A bidirectional link. Fronteirs Mol Neurosci
61. Chen W-W, Chao Y-J, Chang W-H, Chan J-F, Hsu Y-HH (2018) Phosphatidylglycerol incorporates into Cardiolipin to improve mitochondrial activity and inhibits inflammation. Sci Rep 8:4919. https://doi.org/10.1038/s41598-018-23190-z
62. He Y et al (2021) Increased VLCFA-lipids and ELOVL4 underlie neurodegeneration in frontotemporal dementia. Sci Rep 11:21348. https://doi.org/10.1038/s41598-021-00870-x
63. Han X (2010) Multi-dimensional mass spectrometry-based shotgun lipidomics and the altered lipids at the mild cognitive impairment stage of Alzheimer's disease. *Biochimica et Biophysica Acta (BBA) - Molecular and Cell Biology of Lipids*
64. Qiang Liu JZ (2014) Lipid metabolism in alzheimer's disease. Neurosci Bull
65. Hannah Chew VAS (2020) a. A. N. F. Involvement of Lipids in Alzheimer's Disease Pathology and Potential Therapies. *Fronteirs in Physiology*
66. Korbecki J et al (2024) Biochemistry and diseases related to the interconversion of phosphatidylcholine, phosphatidylethanolamine, and phosphatidylserine. Int J Mol Sci 25:10745
67. Alberts B et al (2002) Garland Science,. in *Molecular Biology of the Cell. 4th edition*
68. Liu B, Li Z (2008) Endoplasmic reticulum HSP90b1 (gp96, grp94) optimizes B-cell function via chaperoning integrin and TLR but not Immunoglobulin. Blood J Am Soc Hematol 112:1223–1230
69. Liu B et al (2010) Folding of Toll-like receptors by the HSP90 paralogue gp96 requires a substrate-specific cochaperone. Nat Commun 1:79
70. Bakula D, Scheibye-Knudsen M (2020) MitophAging: mitophagy in aging and disease. Front Cell Dev Biology 8:239
71. Hernández-Ortega K, Garcia-Esparcia P, Gil L, Lucas JJ, Ferrer I (2016) Altered machinery of protein synthesis in alzheimer's: from the nucleolus to the ribosome. Brain Pathol 26:593–605
72. Ding Q, Markesbery WR, Chen Q, Li F, Keller JN (2005) Ribosome dysfunction is an early event in alzheimer's disease. J Neurosci 25:9171–9175
73. Wang X et al (2014) Oxidative stress and mitochondrial dysfunction in alzheimer's disease. Biochim Et Biophys Acta (BBA)-Molecular Basis Disease 1842:1240–1247
74. Seyfried NT et al (2017) A multi-network approach identifies protein-specific co-expression in asymptomatic and symptomatic alzheimer's disease. Cell Syst 4:60–72
75. Song Q, Meng B, Xu H, Mao Z (2020) The emerging roles of vacuolar-type ATPase-dependent lysosomal acidification in neurodegenerative diseases. Translational Neurodegeneration 9:17
76. Mahajan K, Mahajan NP (2015) ACK1/TNK2 tyrosine kinase: molecular signaling and evolving role in cancers. Oncogene 34:4162–4167
77. Nixon RA (2013) The role of autophagy in neurodegenerative disease. Nat Med 19:983–997
78. Zhou Z et al (2021) Downregulation of ATP6V1A involved in Alzheimer's disease via synaptic vesicle cycle, phagosome, and oxidative phosphorylation. *Oxidative medicine and cellular longevity* 5555634 (2021)
79. Conte F, Paci P (2022) Alzheimer's disease: insights from a network medicine perspective. Sci Rep 12:16846
80. Xu A, Kouznetsova VL, Tsigelny IF (2022) Alzheimer's disease diagnostics using Mirna biomarkers and machine learning. J Alzheimer's Disease 86:841–859
81. Lu B. Translational regulation by ribosome-associated quality control in neurodegenerative disease, cancer, and viral infection. Front Cell Dev Biol.10: 970654. 1., Filbeck S, Cerullo F, Pfeffer S, Joazeiro CAP (2022) Ribosome-associated quality-control mechanisms from bacteria to humans. *Mol Cell* 82, 1451–1466 (2022)
82. Ribeiro FC et al (2024) Synaptic proteasome is inhibited in alzheimer's disease models and associates with memory impairment in mice. Alzheimer's Dement 20:e088220
83. Jurcău MC et al (2022) The Link between Oxidative Stress, Mitochondrial Dysfunction and Neuroinflammation in the Pathophysiology of Alzheimer's Disease: Therapeutic Implications and Future Perspectives. Antioxid (Basel) 11. https://doi.org/10.3390/antiox11112167
84. Toledo TM et al (2025) Proteomic analysis of hydrogen peroxide-treated human chondrocytes shows Endoplasmic reticulum stress, cytoskeleton remodeling, and altered secretome composition. Cell Commun Signal 23:282. https://doi.org/10.1186/s12964-025-02291-z
85. Guo Q et al (2023) Fatty acid-binding proteins 3 and 5 are involved in the initiation of mitochondrial damage in ischemic neurons. Redox Biol 59:102547. https://doi.org/10.1016/j.redox.2022.102547
86. Chan RB et al (2012) Comparative lipidomic analysis of mouse and human brain with alzheimer disease. J Biol Chem 287:2678–2688
87. Sharma V, Sharma P, Singh TG (2024) Leukotriene signaling in neurodegeneration: implications for treatment strategies. Inflammopharmacology 32:3571–3584
88. Freeman BA, O'Donnell VB, Schopfer FJ (2018) The discovery of nitro-fatty acids as products of metabolic and inflammatory reactions and mediators of adaptive cell signaling. Nitric Oxide 77:106–111
89. Lee H-T, Lee K-I, Chen C-H, Lee T-S (2019) Genetic deletion of soluble epoxide hydrolase delays the progression of alzheimer's disease. J Neuroinflamm 16:267
90. Tang C et al (2025) Inhibition of soluble epoxide hydrolase ameliorates cerebral blood flow autoregulation and cognition in alzheimer's disease and diabetes-related dementia rat models. Geroscience 47:4429–4449
91. Gregory A, Tang C, Fan F (2025) Soluble epoxide hydrolase: a next-generation drug target for alzheimer's disease and related dementias. Neural Regeneration Res 20:2585–2586
92. Whiley L et al (2014) Evidence of altered phosphatidylcholine metabolism in alzheimer's disease. Neurobiol Aging 35:271–278
93. Han X, Holtzman DM, McKeel DW Jr (2001) Plasmalogen deficiency in early alzheimer's disease subjects and in animal models: molecular characterization using electrospray ionization mass spectrometry. J Neurochem 77:1168–1180
94. Cha YJ et al (2025) Lipidomic network analysis reveals Amyloid-β-Induced lysosomal lipid accumulation in the cortex and hippocampus of 5xFAD mice. J Proteome Res
95. Kim H-E et al (2016) Lipid biosynthesis coordinates a mitochondrial-to-cytosolic stress response. Cell 166:1539–1552e1516
96. Lamari F, Rossignol F, Mitchell GA, Glycerophospholipids (2025) Roles in cell trafficking and associated inborn errors. J Inherit Metab Dis 48:e70019
97. Olsen AS, Færgeman NJ (2017) Sphingolipids: membrane microdomains in brain development, function and neurological diseases. Open Biology 7:170069
98. Lange MLB et al (2008) Loss of phospholipid asymmetry and elevated brain apoptotic protein levels in subjects with amnestic mild cognitive impairment and alzheimer disease. Neurobiol Dis 29:456–464

Publisher's note